

# DISCOL experiment revisited: Assessing the temporal scale of deep-sea mining impacts on sediment biogeochemistry

Laura Haffert<sup>1</sup>, Matthias Haeckel<sup>1</sup>, Henko de Stigter<sup>2</sup> and Felix Janssen<sup>3</sup>

<sup>1</sup> GEOMAR Helmholtz Centre for Ocean Research Kiel, Wischhofstrasse 1-3, 24148 Kiel, Germany

<sup>2</sup> NIOZ - Royal Netherlands Institute for Sea Research and Utrecht University, P.O. Box 59, 1790 AB Den Burg - Texel, The Netherlands

<sup>3</sup> HGF MPG Group for Deep Sea Ecology and Technology at the Max Planck Institute for marine Microbiology, Bremen and Alfred Wegener Institute Helmholtz Centre for Polar and Marine Research, Bremerhaven, Germany  
Max-Planck Institute for marine Microbiology, Bremen, Germany

*Correspondence to:* Laura Haffert (lhaffert@geomar.de)

**Abstract.** Deep-sea mining for polymetallic nodules is expected to have severe environmental impacts because not only nodules, but also benthic fauna and the upper reactive sediment layer are removed through the mining operation, and blanketed by resettling material from the suspended sediment plume. This study aims to provide a holistic assessment of the biogeochemical recovery after a disturbance event by applying prognostic simulations based on an updated diagenetic background model and validated with novel (micro)-biological data. It was found that the recovery strongly depends on the impact type; complete removal of the reactive surface sediment reduces benthic release of nutrients over centuries, while geochemical processes after resuspension and mixing of the surface sediment are near pre-impact state one year after the disturbance. Furthermore, the geochemical impact in the DISCOL area would be mitigated to some degree by a clay-bound Fe(II)-reaction layer, impeding the downward diffusion of oxygen, thus stabilizing the redox zonation of the sediment during transient post-impact recovery. The interdisciplinary (geochemical, numerical and biological) approach highlights the closely linked nature of benthic ecosystem functions, e.g. through bioturbation, microbial biomass and nutrient fluxes, which is also of great importance for the system recovery. It is, however, important to note that the nodule ecosystem may never recover to pre-impact state without the essential hard substrate and will instead be dominated by different faunal communities, functions and services.

## 1 Introduction

This work is part of the JPI Oceans MiningImpact project, which is an integrated research project assessing the potential ecological impact caused by deep-sea mining for polymetallic nodules. Most of these nodules occur in the deep ocean basins at water depths greater than 4000 meter, which represents a part of the ocean that is largely unstudied. In fact, until recently it was assumed that life would be sparse in the deep ocean where, in the absence of light, the only energy source is falling organic matter produced in the photic zone. Increased research interest and technological advances to overcome the large distances and pressure differences of over 400 times the atmospheric pressure have revealed that the deep-sea hosts a surprising diversity of life forms. Information on benthic ecosystem functions, including spatial heterogeneity, temporal variability, and biogeochemical

feedbacks are still limited, but are an important prerequisite in the evaluation of the environmental impacts of deep-sea mining.

This work focuses on a unique study area in the Peru basin (Figure 1), where in 1989 a circular area with a diameter of about 2 nautical miles was intensely disturbed with a plough-harrow as part of the DISturbance and reCOLonization experiment (DISCOL) (Thiel and Schriever, 1990). The DISCOL experimental area (DEA) was revisited before and several times after the initial disturbance, with research concentrating mainly on the characterization and distribution of benthic fauna (Borowski and Thiel, 1998) (Borowski and Thiel, 1998; Borowski, 2001; Bluhm, 2001). Macrofaunal communities, which are particularly important for the bioturbation and thus redox zoning of the sediment, are mainly composed of Polychaeta (about 50%) and to a lesser extent tanaidacea (10 - 20%) and bivalvia (5 – 10%) (Borowski and Thiel, 1998). After the artificial disturbance, very few faunal groups returned to baseline or control conditions after more than two decades (Jones et al., 2017) and the main mode of macrofaunal recolonization was found to be via lateral migration (Borowski and Thiel, 1998). The current MiningImpact project makes use of the technological advances that have taken place in recent years, e.g. precise underwater positioning and in-situ experimentation by remotely operated vehicles (ROVs), in situ oxygen measurement, precise sampling with TV-guided or ROV manipulated equipment and analysis of microbial functions, and attempts to derive a holistic understanding of the deep-sea mining impact on the closely linked ecosystem functions. The specific objectives of this work are:

- (i) Creating a biogeochemical (diagenetic) reference model for the DEA region and validating it based on a comprehensive set of geochemical data (pore water and solid phases from undisturbed and disturbed sediments) obtained with state-of-the-art methodology.
- (ii) Determining short to long-term impacts of a deep-sea mining event on the geochemical system through field data supported simulations.
- (iii) Advancing our understanding on the intricate interplay between ecosystem functions and geochemical processes in the context of a benthic disturbance in the deep sea.

## 2 Methods

### 1.1 Biogeochemical site description

In comparison to other abyssal areas, the Peru basin receives high organic matter input, which is fueled by the equatorial high-productivity zone (Weber et al., 2000). The degradation of deposited organic matter plays a crucial role in defining the benthic biogeochemical system (Froelich et al., 1979). The reactions utilize different terminal electron acceptors in the order of decreasing free-energy production, namely oxygen, nitrate, manganese oxide, iron oxide and sulphate and their availability controls the position of the various redox zones in the sediment column. König et al. (1999), König et al. (2001) and Haeckel et al. (2001) have previously identified and quantified through diagenetic modelling the main biogeochemical processes in the Peru Basin, including the DEA region. They found that organic matter degradation progresses through the stages of oxic respiration, denitrification, manganese and in deeper sediments iron oxide reduction before the reactive fraction of organic matter is diminished leaving only the most refractory fraction of organic material to be permanently buried. Unlike manganese, the reduced Fe(II) species is not released into the porewater but instead incorporated into the clay mineral phase as nontronite resulting in dissolved Fe concentrations below or near detection limit.

75 The largest quantity of organic matter is degraded by oxic respiration in a surface ‘reaction layer’ which  
coincides with the bioturbated zone. Oxygen is depleted in the Peru Basin at a sediment depth of 5 to 15 cm, the  
latter being the typical oxygen penetration depth within the DEA region (Haeckel et al., 2001). Larger variations  
were found among the nitrate profiles. In the slightly shallower region of the Peru Basin seawater-derived nitrate  
and nitrate from oxic respiration are consumed within the bioturbated upper 20 cm of sediment. In contrast, in  
80 the DEA region nitrate escapes the reaction layer and diffuses to a depth of about 2 m, where a Fe(II)-rich layer  
impedes further downward migration (König et al., 2001; see also Figure 2). This Fe(II)-rich layer was formed  
during glacial times (corresponding to an age of at least 60 ka), when organic matter deposition was strongly  
increased and potential electron acceptors such as oxygen, nitrate and manganese oxide were exhausted closely  
below the sediment surface (König et al., 2001). During these times, structural Fe(III) within smectite lattices  
85 acted as the thermodynamically favored electron acceptor, creating Fe(II)-rich surface sediments that were  
subsequently buried (Lyle, 1983). This process was reversed when waning organic matter input during  
interglacial periods allowed oxygen and nitrate to migrate downwards thus creating a ‘burn-down’ situation of  
the redox sensitive Fe(II)-rich smectite phase (Figure 2). The position of the reaction front is easily  
distinguished in deep sediment cores as a transition from a tan to green color change (Lyle, 1983) and has also  
90 been confirmed by Mössbauer spectroscopic measurements (Drodt et al., 1997; König et al., 1997; König et al.,  
1999).

Comparatively little is known about the redox potential of Fe(II) on different crystallographic lattice positions  
(coordination sites) in clay minerals, such as nontronite. In particular, information is lacking on the reactivity of  
the Fe(II) on these sites with respect to oxidation by nitrate and oxygen. Available Mössbauer data (König et al.,  
95 2001) from the DISCOL area indicates a refractory fraction of Fe(II) that prevails in the nitrate reduction zone  
(~10 % of total iron). We propose that part of this refractory fraction is in fact semi-labile and that oxygen,  
which has a higher redox potential than nitrate, can oxidise this semi-labile Fe(II) and thus presents a second  
reaction front impeding the downward migration of oxygen.

## 2.1 Disturbance experiments

100 The current study presents information collected in the DEA during the two legs of the SO242 research cruise in  
2015. The DISCOL experiment was designed to artificially disturb the surface sediment layer through mixing  
and remove nodules from the surface with a specially designed device, the so-called plough-harrow (Thiel and  
Schriever, 1990). To this end the ~4150 m deep circular DEA (11 km<sup>2</sup>) was crossed 78 times starting from  
various directions resulting in a heavily disturbed area in the center and less disturbed peripheral regions. In  
105 total about 20% of the DEA was directly ploughed with the remaining 80% being not directly disturbed but – at  
least in part – covered by an up to 30 mm thick re-settled sediment blanket (Schriever and Thiel, 1992).

During the first leg of SO242 an additional artificial disturbance was created using an epibenthic sled (EBS)  
which was sampled 5 weeks later on the second leg of SO242. The epibenthic sled (CliSAP-Sled; Brenke  
(2005)) has a width of 2.4 m and weight of 880 kg (in air). Unlike the plough-harrow, which ‘mixes’ the upper  
110 sediment layer, the EBS largely scrapes off the upper centimetres of sediment (most of the reactive, bioturbated  
layer), including embedded nodules and bulldozes them sideways from the track.

## 2.2 Sampling procedure

A map of the sampling stations as well as a table of the exact positions are provided in Figure 1 and Table 1, respectively. Several devices were deployed at each sampling site to retrieve surface and subsurface sediment samples (Greinert, 2015; Boetius, 2015): (i) a multiple-corer (MUC, Oktopus, Kiel, Germany), which samples the upper 20 – 40 cm of the sediment including the overlying bottom water; The corer was equipped with a TV-Camera system for precise positioning, e.g. for sampling specific seafloor features like the disturbance tracks; (ii) a ROV-deployed push-corer (PUC) focusing on small-scale topographic features created by the seafloor disturbance; (iii) a box-corer (BC - USNEL type; Hessler and Jumars, 1974) to sample the sediment including macrofauna and nodules; and (iv) a gravity-corer (GC) extracting sediment up to 10 mbsf.

After core retrieval the samples were brought into the ship's cold room (approx. 4 °C). 1 m long sections of the gravity cores were cut into two half cylinders dedicated for sampling and archiving. The working half of the gravity cores were sampled by extracting 3 cm thick slices at intervals of 20 to 40 cm. Sediment from the plastic liners of the other corers were extruded with a piston and cut into 0.5 to 2 cm thick slices under an oxygen-free, argon atmosphere in a glove bag. Subsequently, the pore water was extracted using a low pressure-squeezer (argon gas at 3-5 bar) and filtered through a Nuclepore 0.2 µm polycarbonate filter. Porewater extracted from the samples was stored in two recipient vessels: (i) an acidified sample (i.e. pH<1 with 20 µl 30% HCl suprapur per 1 ml sample) for analysis of metal cations and (ii) a non-acidified sample for nutrients. Additional sediment samples were collected from the same core and sediment intervals for porosity, organic carbon content and radiometric analysis.

## 2.3 Analytical methods

Analyses for the porewater solutes  $\text{NO}_3^-$ ,  $\text{NO}_2^-$ ,  $\text{NH}_4^+$ ,  $\text{PO}_4^{3-}$ ,  $\text{SiO}_4^{4-}$  were completed onboard using a Hitachi UV/VIS spectrophotometer on 1.3 ml of freshly extracted untreated pore water which was diluted 3-fold before analysis. The respective chemical analytics followed standard procedures (Grasshoff et al., 1999), i.e. nitrite and nitrate (after reduction with Cd) were measured as sulphanile-naphthylamide, ammonium was measured as indophenol blue, phosphate and silicate as molybdenum blue, and iron with ferrospectral. The total alkalinity of the porewater was determined by titration with 0.02 N HCl using a mixture of methyl red and methylene blue as indicator. The titration vessel was bubbled with argon to strip any  $\text{CO}_2$  produced during the titration. The IAPSO seawater standard was used for calibration. Further details on analytical methods, e.g. analytical precision and accuracy, are given in Table 2.

At the NIOZ laboratory sediment profiles of  $^{210}\text{Pb}$  and  $^{226}\text{Ra}$ , radio-isotopes from the  $^{234}\text{U}$  decay series were measured in multicores for determining biological mixing rates integrated over a ~100 year time-scale. Total  $^{210}\text{Pb}$  and  $^{226}\text{Ra}$  activity were determined directly by gamma-spectrometry, whilst total  $^{210}\text{Pb}$  was also measured indirectly by alpha-spectrometry via its granddaughter isotope  $^{210}\text{Po}$ . Activities of anthropogenic  $^{137}\text{Cs}$  proved to be generally below detection level. Radionuclide activities are reported in the data base as  $\text{mBq g}^{-1}$  dry sediment.

For gamma-spectrometry, a few grams of freeze-dried and homogenized sediment sample was contained in a 5 cm diameter plastic petri dish, which was closed with tape and sealed gas-tight in a plastic envelope. After leaving the sample for at least 4 weeks to ensure equilibrium, measurement of  $^{210}\text{Pb}$  and  $^{226}\text{Ra}$  were undertaken with a Canberra Broad Energy Range High Purity Germanium Detector (BEGe), using the 46.5 keV line for  $^{210}\text{Pb}$  and 295.2, 351.9 and 609.3 keV lines for  $^{226}\text{Ra}$ . The detector, connected to a computer via a Digital

Spectrum Analyser (DSA-1000), counted the radionuclide activities with Genie 2000 gamma spectroscopy software. The detector was externally calibrated with a Geological Certified Reference Material IAEA/RGU-1, with reference date of 01-01-1988. A monitor standard IAEA-300 provided quality control. Excess  $^{210}\text{Pb}$  activities were calculated by subtracting  $^{226}\text{Ra}$  activity averaged for the 295.2, 351.9 and 609.3 keV lines from the measured total  $^{210}\text{Pb}$  activity.

For alpha spectrometry measurement of  $^{210}\text{Po}$ , 0.5 g of freeze-dried and homogenised sediment sample was spiked with 1 ml of a standard solution of  $^{209}\text{Po}$  in 2M HCl, and then leached for 6 h in 10 ml of concentrated HCl heated to 85°C. After diluting the fluid with 45 ml of demineralised water and adding 5 ml of an aqueous solution of ascorbic acid (40 g L<sup>-1</sup>), natural  $^{210}\text{Po}$  and added  $^{209}\text{Po}$  were collected from the fluid by spontaneous electrochemical deposition on silver plates. For subsequent alpha-spectrometry, Canberra Passivated Implanted Planar Silicon detectors were used.  $^{210}\text{Pb}$  activity was calculated from  $^{210}\text{Po}$ , assuming secular equilibrium and correcting for the time elapsed since collection of the samples.

## 2.4 Numerical methods

We follow the classical approach in early diagenetic modeling where partial differential equations represent the diffusive and advective fluxes coupled to a reaction term ( $R$ ), as formulated by Berner (1980). When applying a conversion via the volume fraction, expressions for solutes and solids can be derived, respectively:

$$\frac{\partial \phi C_{pw}}{\partial t} = \frac{\partial}{\partial x} \left( \phi D \frac{\partial C_{pw}}{\partial x} - \phi u C_{pw} \right) - \phi R(C_{pw}) \quad \text{Eq.(1)}$$

and

$$\frac{\partial (1 - \phi) C_s}{\partial t} = \frac{\partial}{\partial x} \left( (1 - \phi) Db \frac{\partial C_s}{\partial x} - (1 - \phi) w C_s \right) - (1 - \phi) R(C_s) \quad \text{Eq.(2)}$$

where  $t$  and  $x$  represent time and the depth under the seafloor, respectively;  $C_{pw}$  and  $C_s$  are the molar species concentration of solute or solid, respectively;  $\phi$  is the porosity;  $u$  and  $w$  represent fluid and sediment velocity due to burial. Solute diffusion and sediment bioturbation is scaled by the effective diffusion coefficient  $D$  and the bioturbation coefficient  $Db$ .

The porosity-depth profile is assumed to be produced by steady-state compaction (Berner, 1980) and is approximated empirically by the following exponential function (Murray et al., 1978; Berner, 1980; Martin et al., 1991; Rabouille and Gaillard, 1991b, a):

$$\phi(x) = \phi_{\infty} + (\phi_0 - \phi_{\infty}) e^{-\beta x} \quad \text{Eq.(3)}$$

where  $\phi_{\infty}$  is the porosity at infinite depth,  $\phi_0$  is the porosity at the sediment surface ( $x=0$ ) and  $\beta$  is the porosity attenuation coefficient.

The fluid and sediment velocity-depth distribution is calculated according to the mathematical convention of Luff and Wallmann (2003):

$$u(x) = \frac{\phi_{\infty} w_{\infty}}{\phi(x)} \quad \text{Eq.(4)}$$

and

$$w(x) = \frac{1 - \phi_{\infty}}{1 - \phi(x)} w_{\infty} \quad \text{Eq.(5)}$$

where  $w_{\infty}$  is the burial velocity at infinite depth.

The effective diffusion coefficient was tortuosity corrected:

$$D(x) = \frac{D^o(x)}{\theta^2(x)} \quad \text{Eq.(6)}$$

with  $D_0$  being the infinite dilution molecular diffusion coefficient calculated after Berner (1980) and  $\theta^2$  being the squared tortuosity. The tortuosity can be related to the porosity  $\phi$  according to Boudreau (1996):

$$\theta^2(x) = 1 - 2 \ln \phi(x) \quad \text{Eq.(7)}$$

185 The bioturbation profile is approximated by the arbitrary function:

$$Db = Db^0 \cdot 0.5 \operatorname{erfc}\left(\frac{x - x_{Db}}{\beta_{Db}}\right) \quad \text{Eq.(8)}$$

Where  $Db^0$  represents the maximum bioturbation intensity at the sediment surface,  $x_{Db}$  is the bioturbation half depth and  $\beta_{Db}$  the bioturbation attenuation coefficient.

The diagenetic equations, consisting of a set of partial differential equations (Equation 1 and 2), are solved via a finite difference scheme (1D uneven grid with a sigmoidal distribution ranging from 0.1 cm at the surface and 1  
190 cm at the lower boundary) and subsequent minimization of the ordinary differential equations by inbuilt ODE solvers of MATLAB.

The reaction network shaping the geochemistry of the upper sediment metres, namely organic matter degradation and secondary redox reactions including the oxidation of ammonium and dissolved manganese, are listed in Table 3 as well as the corresponding rate expressions. To account for different reactivities of the  
195 various organic matter phases, we apply a 3G model (Jorgensen, 1978; Westrich and Berner, 1984; Middelburg, 1989) allowing for a labile, moderately reactive and a refractory phase. We also included a shallow semi-labile Fe(II) layer that reacts with oxygen to the model (Figure 2). While it is established that a labile Fe(II) reaction front impedes the downward migration of nitrate (König et al., 1997; König et al., 1999), little is known about the redox potential of Fe(II) on different crystallographic lattice positions (coordination sites) in clay minerals,  
200 such as nontronite. In particular, information is lacking on the reactivity of the Fe(II) on these sites with respect to oxidation by nitrate and oxygen. Available Mößbauer data (König et al., 2001) from the DISCOL area indicate a refractory fraction of Fe(II) that prevails in the nitrate reduction zone (~10 % of total iron). In the light of the much higher redox potential of oxygen compared to nitrate, we model the remaining Fe(II) as a semi-labile phase representing a second reaction front impeding the downward migration of oxygen. The diagenetic  
205 model is applied to define a background or reference geochemical system. This is then used to derive transient prognostic models in response to different impact types. Initial profiles of the transient simulations are based on the steady state background model which were adjusted for the modelled impact type: (i) in the case of ‘sediment removal’, the top 10 cm of the background profiles were ‘cut off’ while maintaining bottom water concentrations and organic matter flux for the upper boundary conditions. For the ‘sediment mixing’ case, the  
210 oxygen concentrations of the upper 10 cm of the sediment were set to bottom water values, imitating an oxygen flooding event. Transient models were augmented by an additional Fe(II) profile - an oxygen reaction layer (Figure 2) - as justified by the surprisingly constant oxygen penetration depth at the reference and all disturbed sites. This Fe(II) reaction layer is crucial in the prognostic simulations which would otherwise predict that oxygen rapidly diffuses into deeper sediments after a disturbance event. It is assumed that bioturbation is  
215 inhibited immediately after the impact with a linear increase to undisturbed reference bioturbation intensity within 100 to 200 years, which is in line with macrofaunal abundance data presented in Stratmann et al. (2018a). A detailed parameterization of the background and prognostic models is provided in Table 4.

The bioturbation coefficient  $Db^0$ , a critical input parameter to the background model, is derived by fitting a simplified version of the background model to summed  $^{210}\text{Pb}$ ,  $^{226}\text{Ra}$  and  $^{230}\text{Th}$  radiometric data. The physical set up of the model is the same as the background model with the difference that only the above mentioned radiometric species and their first order radioactive decay is considered.

### 3 Results

#### 3.1 Geochemistry of the DEA region

The parameter depth profiles for each core are presented in Figure 3 – 6, grouped in ‘outside DEA’ and ‘inside DEA’ stations for the gravity cores and for the multiple and box cores in reference sites and various types of disturbed sites.

Geochemical trends observed in the sediment cores from reference stations agree in general well with those observed in the same area during a previous investigation (Haeckel et al., 2001). The upper reactive sediment section (up to ~20 cm.b.s.f) is markedly different from the deeper sediment sections (up to 10 m) (Figure 3). It is characterized by a significant decrease in porosity (from 0.94 to approx. 0.86, Table 4 and Figure 4) and is rich in manganese oxides (1 - 2 wt%, Paul et al., 2019), which gives this layer its distinct dark brown color. Below this layer, the sediment takes on a light brown to grey brown (tan) color, which is replaced by a grayish green color - the shift to Fe(II)-rich lattices in the smectite phase – at a depth of 2 – 2.5 m (38GC1, 84GC3, 100GC5, and 123GC6, Table 1). Organic carbon content in the DEA region oscillates about a mean value of 0.5 to 0.75 wt% in the upper 50 cm (Figure 3), which is controlled by the difference in organic carbon input during glacial (higher  $C_{\text{org}}$  content) and interglacial (lower  $C_{\text{org}}$  content) sedimentation regimes (Haeckel et al., 2001). With depth the organic carbon content decreases steadily to about 0.1 wt% at 10 m.b.s.f (Figure 3). Contrary to previous observations that nodules in the DEA area occur only at the sediment surface, investigation of the current set of gravity cores revealed buried manganese nodules at depths of 4 to 8 m (Figure 3). The undisturbed appearance of the sediment surrounding these buried nodules, and evidence of diagenetic alteration of the nodules, proves that these nodules were genuinely buried and do not represent a coring artifact.

In situ oxygen profiles confirm that the upper brown layer represents the oxygenated zone (Figure 5). In this zone, oxic respiration of organic matter not only consumes downward diffusing oxygen but increases ammonium and, via nitrification, also nitrate (Figure 6). While the trend in the nitrate profiles is clearly discernable, ammonium concentrations remain rather low (10 – 20  $\mu\text{mol/l}$ ) and are scattered and are likely controlled by secondary processes, such as adsorption and desorption (Haeckel et al., 2001). Below the oxic dark brown layer, denitrification commences and nitrate declines within the upper 2 -3 m of the sediment and is entirely depleted in the cores with the greyish green Fe(II)-rich reaction layer (51GC2, 84GC3, 100GC5, 123GC6, Figure 3). The depleted nitrate profiles tend to be more linear (e.g. 84GC3) than the profiles of cores where the Fe(II)-rich layer is absent (e.g. 132GC7), as is typical in the presence of a reaction layer (Goloway and Bender, 1982; Wilson et al., 1985; Jahnke et al., 1989). Dissolved manganese is strongly redox sensitive and is absent in the upper oxic zone (Figure 6). Below the oxic zone, organic matter degradation progresses to manganese oxide reduction and produces dissolved manganese, which increases steadily until it reaches an asymptotic concentration at 6 m depth with terminal concentrations ranging between 25 and 120  $\mu\text{mol/l}$  (Figure 3). Diagenetic simulations (Haeckel et al., 2001) could not reproduce this strong increase in dissolved

manganese and the discovery of buried manganese nodules now confirms that the dissolved manganese concentrations are indeed additionally shaped by the dissolution of manganese nodules at a depth of 4 – 8 m.

Alkalinity profiles are largely unchanged over the entire sampling domain (up to 10 m), but display some variations in the upper 5 cm (Figure 6). Haeckel et al. (2001) have argued that the alkalinity profile is likely influenced by carbonate geochemistry, so we will neglect the upper alkalinity profile in our interpretations. Dissolved iron concentrations were near or below the detection limit of 1  $\mu\text{M}$  in all cores due to its incorporation into the clay mineral phase and sulphate concentrations remained close to their sea water value, which is in line with the absence of sulfate reduction in the Peru basin.

### 3.2 Diagenetic reference model

With the MiningImpact sampling campaign specifically targeting the DEA region, we were able to update the parameterization of the previous model presented by Haeckel et al. (2001). The main differences are: (i) The presented model applies a 3G-model, i.e. allows for three fractions of organic matter with varying reactivity, and thus a better fit to the field data. And (ii) The bioturbation intensity ( $D_B = 0.65 \text{ cm}^2 \text{ a}^{-1}$ ) and depth profile are now based on radioactive disequilibria between radionuclides of the natural uranium and thorium series in the DEA region (Figure 7). The numerical simulations predict that excess  $^{210}\text{Pb}$  (difference between solid and dashed lines) exists down to ~10 cm and below the measured activity is supported by  $^{230}\text{Th}$  (dotted line) and  $^{226}\text{Ra}$  (difference between dashed and dotted lines). A relatively high scatter of radioactive activities of 1.5-3 Bq/g was observed in the uppermost sediment samples (0-0.5 cm) reflecting lateral inhomogeneities. These could be due to sediment focusing created by local topography, e.g. small depressions acting as deposition centers for fluffy material or by ‘hotspots’ of non-local mixing by individual organisms.

A satisfactory background model fit to undisturbed reference sites could be achieved for all relevant parameters with particular focus being placed on accurately simulating the redox zonation of the sediment, especially the oxygen penetration depth and the concurrent increase in dissolved manganese (Figure 8). It should be noted that the geochemical state of the Peru basin is likely transient in nature arising from long-term (glacial/interglacial) as well as short-term (ENSO time scale) variations in the depositional flux of organic matter (König et al., 2001). This work focuses on modelling the biogeochemical processes in the upper half meter of the sediment, which are defined by the Holocene organic matter input, and are thus unaffected by long-term changes in the depositional flux. Similar to the downward migrating nitrate front, it is likely that the pore water oxygen content also increases with currently waning organic matter input. The analytical oxygen profiles display less curvature (more linearity) than the modelled profiles, which suggests that secondary reactions, such as a semi-labile Fe(II)-oxygen reaction front, additionally shape the oxygen profile. However, due to the uncertainty in a transient parameterization, we model the reference sediments as a steady state scenario - justified by the generally good agreement of the model with the geochemical data.

### 3.3 Impact characterization

All sample stations were affected by at least one of the following processes: (i) removal of the upper dark brown reactive layer, (ii) mixing and redistribution of the surface sediment resulting in piling up (‘riges’) and removal (‘furrows’), (iii) turning of the upper sediment upside down or bringing up deep sediment to the surface – both leading to exposure of sediment from below the reactive layer at the surface and (iv) deposition of re-suspended sediment. Furthermore, there were distinct differences in the physical impact of the plough-harrow and EBS



295 track. While the EBS scraped off the surface sediments and relocated them to the side of the track, the plough-harrow mixed and displaced sediments resulting in a variety of disturbance structures. In the following a detailed description of the physical and geochemical impact is provided and will be complemented by information on the microbiological impact from a parallel study (Vonnahme et al., in press).

300 Sediments inside the EBS track are largely devoid of the upper reactive brown layer, exposing the tan-colored subsurface sediment in places. The surface of the track is smooth indicating that sediment mixing is negligible inside the tracks. Removal of the upper reactive layer resulted in decreased sediment porosity by exposing more compacted sediment compared to the reference sites and brought the boundary below which dissolved manganese is found in the sediment pore water as close as 5 cm bsf. (Figure 4 and 6). In contrast, the oxygen penetration depth does not vary significantly from the reference area, the profile shape is however slightly more linear (Figure 5). In line with the severe disturbance of the sediment, physical signs of bioturbation (recent bioturbation channels connected to the surface) are lacking and the microbial cell count in the surface sediment is reduced by 50% with the microbial communities being significantly different from the reference sites (Vonnahme et al., in press).

310 The disturbance of the surface sediment layer brought about during the DISCOL experiment were still clearly visible after 26 years and the TV-guided sampling campaign was able to specifically target the following features: (i) The area next to the plough-harrow track ('outside track'), that is not mechanically disturbed but affected by resettling sediment from the disturbance plume. Geochemical profiles do not indicate a significant difference to the reference site (Figure 6), especially with the natural heterogeneity of the area in mind. Differences in the microbial functions compared to the reference stations are also within the methods' confidence level and recent bioturbation confirms that the sediment is presently colonized by burying macrofauna (Vonnahme et al., in press). (ii) The furrows drawn in the seabed by the plough-harrow show some distinct differences to the reference sites. The reactive dark brown surface layer is reduced in thickness and is overlain by re-settling sediment which preferentially accumulated in the depression. While geochemical profiles do not differ significantly from the reference site, biological processes are noticeably decreased (Vonnahme et al., in press). (iii) 'Ridge' sediments show the same disturbance effects, albeit more severe, and seafloor integrity is compromised by deep cracks throughout the sediment (Vonnahme et al., in press). (iv) Exposed subsurface sediment observable as lighter-coloured patches show the highest level of disturbance, similar in character to the fresh surface created by the EBS. The reactive brown layer is absent and thus the porosity of the surface sediment reduced (Figure 4). Biological processes are significantly impacted. Bioturbation channels are scarce and disconnected with the surface, indicating a pre-impact origin. Microbial cell numbers are reduced by 30% with the microbial communities being more similar to those of the subsurface sediment (14-16 cm.b.s.f.) of the reference stations than those of the surface sediments (Vonnahme et al., in press).

### 3.4 Prognostic simulations

330 The following presentation of simulation results focuses on the distribution of oxygen, which plays a central role in biogeochemical processes: Different impact types were simulated by two 'end member' scenarios. The first scenario assumes that 10 cm of the upper sediment were removed, i.e. the first 10 cm of the reference steady-state profiles were discarded, exposing anoxic subsurface sediments to bottom water concentrations. The second scenario floods the upper 10 cm of the sediment with oxygen, representing, on one hand, the effect of sediment mixing and cracking and, on the other, the effect of re-suspension and subsequent settling of freshly oxygenated

335 reactive sediment (Figure 9). The transient models showed that the impact of the removal of the reactive upper 10 cm layer is much more severe and longer lasting compared to the 'oxygen flooding' scenario. And simulations show no distinguishable difference if 8 or 12 cm are removed instead of 10. This is because the greatest disturbance effect is caused by the absence of the labile organic matter fraction, which is restricted mostly to the upper 10 centimetres of the sediment.

340 *Short term impact.* Immediately after the removal of the highly reactive surface sediment, solute profiles are in strong disequilibrium and mostly diffusion controlled. This is especially true for oxygen, which rapidly diffuses into previously anoxic sediments. The Fe(II) layer plays an insignificant role in the initial post-impact weeks but commences to inhibit further penetration of the oxygen front at 5 weeks. In the absence of the reactive surface layer, organic matter degradation rates, which strongly shape the reference oxygen profile, play only a minimal  
345 role in the weeks after the disturbance. The modelled 'removal' profiles agree well with the analytical in situ oxygen profiles of the 5 week old EBS track and confirm that the linear nature of the analytical profiles is likely shaped by a mixture of a downward diffusing oxygen front and the initiation of the oxygen-Fe(II) reaction layer. For comparison, impact simulations assuming full recovery of the bioturbation intensity by 200 years instead of 100 years, are also shown. Here, the oxygen profile is also distinctly more linear but even more reduced  
350 sediment mixing through bioturbation allows oxygen to penetrate slightly deeper (18 cm.b.s.f.) compared to the in situ oxygen profiles (13 cm) and to the 100 year bioturbation recovery interval (10 cm.b.s.f, Figure 10).

The 'oxygen flooding' scenario produces a very different oxygen profile. It is shaped mainly by the reaction of the anomalous oxygen with the reactive (labile) organic matter, especially in the upper centimeters where the labile organic matter is most concentrated. The difference to the EBS track in situ profiles supports the  
355 observation that the EBS track is mainly affected by sediment removal, rather than mixing (Figure 11).

*Medium term impact.* The existence of the Fe(II)-oxygen reaction layer plays a particularly important role in the decades after the disturbance. Oxygen is less efficiently removed from the pore water in both scenarios: Removal of the reactive layer significantly reduces oxygen uptake through organic matter degradation and the reactivity of the organic matter was reduced due to reaction with the anomalous flooding with oxygen. In the  
360 absence of an oxygen impeding reaction layer, oxygen penetration depths would consequently be significantly increased in both cases (Figure 10 and 11). Simulating the 26 year old DISCOL disturbance has shown that the existence of an oxygen consuming reaction layer is a necessary prerequisite. The 'removal scenario' produces slightly more linear profiles compared to the 'oxygen flooding' simulation because of the relative importance of the Fe(II)-oxygen reaction layer over organic matter degradation process. The slight misfit of both scenarios  
365 with the in situ oxygen data suggests that the DEA tracks are most likely affected by a mixture of both scenarios, possible leveled out by lateral diffusion effects. Ongoing organic matter flux at the surface sediment builds up a new post-impact reactive layer with reactivities higher than in the reference model due to the ineffective mixing into deeper sediments through bioturbation (Figure 10 and 11). Thus, differences between bioturbation recovery scenarios, i.e. 100 and 200 years, increase over time with an increasing amount of fresh  
370 organic matter that can potentially be mixed into the sediment.

*Long term impact.* It takes centuries for the geochemical processes to completely recover after the removal of the upper reactive sediment. While the observed geochemical profiles of the disturbed sites show surprisingly little variation compared to the reference site, overall surface fluxes vary significantly during the first 100 years after the impact. This is especially true for the oxygen flux into the sediment, which is more than halved within

the first year of the impact (Figure 10). Within the first decades after the impact the build-up of the labile organic matter, and its mixing into deeper sediment through bioturbation, gains influence. With increasing depletion of oxygen through organic matter degradation, oxygen concentrations decrease alongside with Fe(II)-oxygen reaction rates. The transition from Fe(II)-controlled to organic matter-controlled oxygen profiles is accompanied by a slight increase in the oxygen penetration depth (Figure 10). The exact quantification of this transition is difficult to estimate, but the fact that 26 years after the impact oxygen profiles are still efficiently impeded by the Fe(II)-oxygen reaction layer suggests that this process will significantly reduce the oxygen penetration depth until the organic matter degradation rates are near pre-disturbance levels (ca. 100 years after the impact). Interestingly, while steady-state biogeochemical processes strongly depend on the depth and intensity of bioturbation (Haeckel et al., 2001), the time frame of the bioturbation recovery has very little influence on the overall impact recovery process (Figure 10). This is due to the fact, that the limiting factor is the availability of labile organic matter, which is replenished on a much longer time scale compared to the faunal recovery (Stratmann et al., 2018a).

Recovery of the sediment that was affected by the ‘oxygen flooding’ scenario is occurring within 100 years and is already in a near pre-impact state 1 year after the disturbance. Here, the Fe(II)-oxygen reaction layer is predominantly responsible for restricting the anomalously high oxygen levels within the upper 20 cm of the sediment. Organic matter degradation rates remain high throughout the recovery process and build-up of fresh labile organic matter that replenishes the loss through the introduction of anomalous oxygen concentration occurs within the recovery phase of the bioturbation (Figure 11).

#### 4. Discussion

The benthic ecosystem is shaped by a balanced interplay of physical, chemical and biological factors, which are fueled by the deposition of organic matter, especially its labile fraction (Figure 12): The degradation of organic matter is microbially catalyzed and in turn provides nutrients to the microbial community (e.g. Witte et al., 2003a; Moodley et al., 2005; Stratmann et al., 2018b; Sweetman et al., 2018). The associated microbial growth provides biomass that sustains meio and macrofauna and forms an important component of the benthic food web (Witte et al., 2003b; Van Oevelen et al., 2006; Van Oevelen et al., 2011). The concomitant bioturbation of the sediment induces a variety of changes, such as lowering the sediment shear strength and the vertical transport of fresh reactive organic matter into deeper sediments (bioturbation) through burrowing invertebrates (Krantzberg, 1985, and references therein). The occurrence of labile organic matter in deeper sediments where oxygen is not as easily replenished compared to surface sediments places an important restriction on the oxygen penetration depth (Haeckel et al., 2001). Bioturbation plays thus a deciding factor in early-diagenetic, especially redox sensitive, processes. These are typically closely linked to the microbial functions and with the introduction of fresh and digested organic matter at depth by infauna new material for additional degradation and microbial colonization, close the causal cycle (Levin et al., 1997; Witte et al., 2003a; Middelburg, 2018). Changes in any compartment of the ecosystem functions will entail modifications of all biogeochemical processes. A natural example is the long-term glacial/interglacial or short-term ENSO driven change in the depositional flux of organic matter to the seafloor imposing gradual cycles in the redox zonation of the sediment (König et al., 2001).

Mining the seafloor will have an abrupt and direct impact on several benthic ecosystem functions at a time: (i) through the removal of all seafloor fauna (Vanreusel et al., 2016; Jones et al., 2017; Gollner et al., 2017; Bluhm, 2001; Borowski, 2001), (ii) through changing the physical characteristics of the sediment surface, i.e. by exposing more compacted sediments with increased shear strength, and removing manganese nodules as hard-substrate habitats (Grupe et al., 2001) and (iii) through the displacement and removal of labile organic matter.

Biological, geochemical and numerical results of the MiningImpact project significantly improve our understanding of the interlinked ecosystem recovery processes in the deep-sea. Removal of the upper reactive surface layer and its fauna will halt bioturbation and organic degradation rates and significantly decrease microbial activity (Figure 12A and B). Based only on deep-sea typical microbial biomass turnover rates and conservative bacterial doubling times, recovery of microbial abundances should occur within 2 – 10 years. Observations show, however, that the microbial activity remained significantly reduced in the decades following the DISCOL disturbance experiment (Vonnahme et al., in press). Microbial recovery thus appears controlled by the re-establishment of the labile organic matter fraction, which is still significantly reduced at this times scale. Low nutrient fluxes and the downsized microbial biomass cannot sustain pre-impact faunal abundances (Stratmann et al., 2018a), and recolonization is obstructed by the comparatively hard substrate and absence of hard-substrate habitats (nodule surface) in impacted areas (Vonnahme et al., in press). This directly affects the macrofaunal efficiency to mix surface sediments into deeper layers which is presented in the simulations by the reduced bioturbation coefficient (Figure 12). It should be noted that even if sediment physical conditions and organic matter availability have recovered, it is unclear whether the pre-impact infauna is still available to recolonize the disturbed area.

Prognostic simulations showed that the time scale of the ecosystem recovery ultimately depends only on one factor: the availability of labile organic matter. The amount of reactive organic matter determines the intensity of the food-web activity (i.e. summed carbon cycling, Stratmann et al. (2018a)) and has to reach pre-impact levels to allow for the interlinked ecosystem to recover. In this context, two aspects should be particularly emphasized: (i) deep-sea sediments are characterized by extremely low surface sedimentation rates (~0.004 cm/a) and thus organic matter influx, so that complete recovery of the labile organic matter fraction takes up to 1000 years (Figure 12). In the Clarion-Clipperton Zone, located also in the abyssal plains of the Pacific Ocean, surface sedimentation rates are even lower (0.0002 – 0.001 cm/a; Volz et al. (2018)). In this area, where nodule mining is expected to commence, potential impact recovery after removal of the upper reactive layer was predicted to occur on an even longer (millennia) time scale (Volz et al., under review). (ii) Ecosystem impact and consequent recovery is strongly dependent on the type of disturbance, more precisely, on the amount of labile organic matter removed. Microbial activity at disturbed sites could be directly correlated to an arbitrary disturbance gradient (Vonnahme et al., in press), which in turn coincides with the thickness of the reactive dark brown surface sediments that was removed during the experimental disturbance. These findings are in line with the results of the prognostic simulations, which showed that the impact is much less severe and recovery times significantly reduced (decades, Figure 11) if sediments are simply mixed or affected by resettling sediment ('oxygen flooding' scenario), compared to the removal of the upper reactive layer (centuries, Figure 10 and 12).

## 5. Conclusions

Previous diagenetic models of the DEA (Haeckel et al., 2001) were updated by a field-based bioturbation coefficient and application of a 3G-organic matter model. A near-surface Fe(II)-oxygen reaction layer was introduced in the prognostic simulations, which represents the refractory Fe(II) phase that did not react with the downward progressing interglacial nitrate front. The surprisingly similar oxygen penetration depths in reference and 26 year old disturbed sediments indicates that this refractory Fe(II) appears to be an efficient barrier for the progressing oxygen front thus defying previous impact simulation that predicted a significant downward migration of the oxygen front (König et al., 2001).

Transient simulation results have significantly enhanced the quality of the interpretation of the observed geochemical profiles, which on first sight do not exhibit marked differences among the various disturbed and reference sites. The geochemical recovery after a mining related removal of the upper reactive sediment layer can be divided into three stages: (i) the initial diffusion driven equilibration of the post-impact profiles (within weeks of the impact), (ii) burn down of the Fe(II)-oxygen reaction layer (decades after the impact) and (iii) re-establishment of the reactive organic matter layer (centuries after the impact). If the reactive surface sediment is not removed but instead mixed or temporarily re-suspended, anomalously high oxygen concentrations alter biogeochemical processes on a decadal scale, albeit much less severe.

The interdisciplinary (geochemical, numerical and biological) approach to characterise the impact of benthic disturbances on early diagenetic processes provided valuable information on post-impact processes. On one hand it identifies variables that are suitable as indicators of benthic ecosystem health and also allow identification of significant adverse change of the benthic environment. Metabolites of microbial activity were found to be particularly sensitive to disturbances and can even resolve grades of impact (Vonnahme et al., in press). Biogeochemical processes responded more subtle to the disturbance with oxygen, nitrite and bioturbation activity being the most suitable variables. On the other hand, this work highlights the closely linked nature of different benthic ecosystem functions, which is also true during the recovery from mining impacts. The main factor constraining the time frame of the geochemical recovery is the availability of reactive (labile) organic matter, emphasizing the importance of the impact type (sediment removal versus mixing and resuspension) and also the natural depositional flux of organic matter onto the sediment surface (e.g. DEA versus the Clarion-Clipperton Zone). The microbial degradation of the available reactive organic matter fraction defines the base of the food web structure, which eventually sustains metazoans. Some of the epifauna burrows into the seafloor (bioturbation) and in turn has a critical influence on geochemical, especially redox sensitive, processes and fluxes. Recovery of the system is thus only possible if the ecosystem functions of all compartments are restored. Our results also show that it is important to identify regional features, such as the reactive Fe(II) layer in DISCOL sediments, because they may affect the biogeochemical response to a benthic disturbance drastically.

While biogeochemical fluxes may recover close to the pre-impact state, the nodule ecosystem cannot recover, since the essential hard substrate, the polymetallic nodules, have been removed. Consequently, a new nodule-free ecosystem with very different faunal communities, functions and services has to establish in the mining areas and its thickly blanketed surrounding. Furthermore, this new ecosystem will take much longer time scales to establish because it is largely controlled by the recovery of the underlying biogeochemical fluxes and processes that fuel abyssal life.

## Acknowledgements

The authors would like to thank A. Bleyer, R. Surberg, B. Domeyer and K. Hamann for co-working on sample collection on RV Sonne and onboard and onshore pore water analyses. P. van Gaever is thanked for carrying out the radionuclide analysis. We are also indebted to the captain and crew of RV SONNE for their invaluable support during the cruise SO242. We are grateful for the constructive comments of two anonymous reviewers. This work was funded by the German Federal Ministry of Education and Research through the MiningImpact project (grant no. 03F0707A, 03F0707D, 03F0812A and 03F0812D) of the Joint Programming Initiative of Healthy and Productive Seas and Oceans (JPIO). The authors are solely responsible for the content of this paper.

## Data availability

The geochemical data presented in Figure 3, 4 and 6 are publically available in the PANGAEA database with the DOI <https://doi.org/10.1594/PANGAEA.905377>. The PANGAEA database also hosts the activity measurements of the  $^{210}\text{Pb}$  series presented Figure 7 with the DOIs <https://doi.org/10.1594/PANGAEA.905442> (alpha spectrometry) and <https://doi.org/10.1594/PANGAEA.905443> (gamma spectrometry).

## References

- Berner, R. A.: Early Diagenesis - A Theoretical Approach, Princeton University Press, Princeton, New Jersey, 241 pp., 1980.
- Bluhm, H.: Re-establishment of an abyssal megabenthic community after experimental physical disturbance of the seafloor, Deep-Sea Research Part II-Topical Studies in Oceanography, 48, 3841-3868, Doi 10.1016/S0967-0645(01)00070-4, 2001.
- Boetius, A.: RV SONNE Cruise Report SO242-2: JPI OCEANS Ecological Aspects of Deep-Sea Mining, DISCOL Revisited, 2015.
- Borowski, C., and Thiel, H.: Deep-sea macrofaunal impacts of a large-scale physical disturbance experiment in the Southeast Pacific, Deep Sea Research Part II: Topical Studies in Oceanography, 45, 55-81, 10.1016/S0967-0645(97)00073-8, 1998.
- Borowski, C.: Physically disturbed deep-sea macrofauna in the Peru Basin, southeast Pacific, revisited 7 years after the experimental impact, Deep-Sea Research II, 48, 3809-3839, 2001.
- Boudreau, B. P.: Diagenetic Models and Their Implementation: Modelling Transport and Reactions in Aquatic Sediments, Springer-Verlag, Berlin, Heidelberg, New York, 414 pp., 1996.
- Brelaud, J., and Byrne, R.: Spectrophotometric procedures for determination of sea water alkalinity using bromocresol green, Deep-Sea Research I, 40, 629-641, 1993.
- Brenke, N.: An Epibenthic sledge for operations on marine soft bottom and bedrock, Marine Technology Society Journal, 39, 10-21, Doi 10.4031/002533205787444015, 2005.
- Drodt, M., Trautwein, A. X., König, I., Suess, E., and Koch, C. B.: Mössbauer spectroscopic studies on the iron forms of deep-sea sediments, Physics and Chemistry of Minerals, 24, 281-293, 10.1007/s002690050040, 1997.
- Froelich, P. N., Klinkhammer, G. P., Bender, M. L., Luedtke, N. A., Heath, G. R., Cullen, D., Dauphin, P., Hammond, D., Hartman, B., and Maynard, V.: Early oxidation of organic matter in pelagic sediments of the eastern equatorial Atlantic: suboxic diagenesis, Geochimica et Cosmochimica Acta, 43, 1075-1090, 1979.
- Gollner, S., Kaiser, S., Menzel, L., Jones, D. O. B., Brown, A., Mestre, N. C., van Oevelen, D., Menot, L., Colaco, A., Canals, M., Cuvelier, D., Durden, J. M., Gebruk, A., Egho, G. A., Haeckel, M., Marcon, Y., Mevenkamp, L., Morato, T., Pham, C. K., Purser, A., Sanchez-Vidal, A., Vanreusel, A., Vink, A., and Martinez Arbizu, P.: Resilience of benthic deep-sea fauna to mining activities, Mar Environ Res, 129, 76-101, 10.1016/j.marenvres.2017.04.010, 2017.
- Goloway, F., and Bender, M.: Diagenetic models of interstitial nitrate profiles in deep sea suboxic sediments, Limnology and Oceanography, 27, 624-638, 1982.
- Grasshoff, K., Ehrhardt, M., and Kremling, K.: Methods of Seawater Analysis, 3 ed., Wiley-VCH, Weinheim, 600 pp. pp., 1999.

Greinert, J.: RV SONNE Cruise Report SO242-1 JPI OCEANS Ecological Aspects of Deep-Sea Mining DISCOL Revisited, GEOMAR, 2015.

540 Grupe, B., Becker, H. J., and Oebius, H. U.: Geotechnical and sedimentological investigations of deep-sea sediments from a manganese nodule field of the Peru Basin, Deep Sea Research Part II: Topical Studies in Oceanography, 48, 3593-3608, 10.1016/s0967-0645(01)00058-3, 2001.

Haeckel, M., König, I., Riech, V., Weber, M., and Suess, E.: Pore water profiles and numerical modelling of Peru Basin deep-sea sediments, Deep-Sea Research II, 48, 3713-3736, 2001.

545 Hessler, R. R., and Jumars, P. A.: Abyssal community analysis from replicate box cores in the central North Pacific, Deep-Sea Research I, 21, 185-209, 1974.

Jahnke, R. A., Emerson, S. R., Reimers, C. E., Schuffert, J., Ruttenger, K., and Archer, D.: Benthic recycling of biogenic debris in the eastern tropical Atlantic Ocean, Geochimica et Cosmochimica Acta, 53, 2947-2960, 1989.

550 Jones, D. O., Kaiser, S., Sweetman, A. K., Smith, C. R., Menot, L., Vink, A., Trueblood, D., Greinert, J., Billett, D. S., Arbizu, P. M., Radziejewska, T., Singh, R., Ingole, B., Stratmann, T., Simon-Lledo, E., Durden, J. M., and Clark, M. R.: Biological responses to disturbance from simulated deep-sea polymetallic nodule mining, PLoS One, 12, e0171750, 10.1371/journal.pone.0171750, 2017.

Jorgensen, B. B.: A comparison of methods for the quantification of bacterial sulfate reduction in coastal marine sediments. II. Calculation from mathematical models, Geomicrobiology Journal, 1, 29-47, 10.1080/01490457809377722, 1978.

König, I., Drodt, M., Suess, E., and Trautwein, A. X.: Iron reduction through the tan-green color transition in deep-sea sediments, Geochimica et Cosmochimica Acta, 61, 1679-1683, 1997.

560 König, I., Haeckel, M., Drodt, M., Suess, E., and Trautwein, A. X.: Reactive Fe(II) layers in deep-sea sediments, Geochimica et Cosmochimica Acta, 63, 1517-1526, 1999.

König, I., Haeckel, M., Lougear, A., Suess, E., and Trautwein, A. X.: A geochemical model of the Peru Basin deep-sea floor and the response of the system to technical impacts, Deep-Sea Research II, 48, 3737-3756, 2001.

565 Krantzberg, G.: The Influence of Bioturbation on Physical, Chemical and Biological Parameters in Aquatic Environments: A Review Environmental Pollution (Series A), 39, 99-122, 1985.

Levin, L., Blair, N., DeMaster, D., Plaia, G., Fornes, W., Martin, C., and Thomas, C.: Rapid subduction of organic matter by maldanid polychaetes on the North Carolina slope, Journal of Marine Research, 55, 595-611, 1997.

570 Luff, R., and Wallmann, K.: Fluid flow, methane fluxes, carbonate precipitation and biogeochemical turnover in gas hydrate-bearing sediments at Hydrate Ridge, Cascadia Margin: Numerical modeling and mass balances, Geochimica et Cosmochimica Acta, 67, 3403-3421, 2003.

Lyle, M.: The brown-green color transition in marine sediments: A marker of the Fe(III)-Fe(II) redox boundary, Limnology and Oceanography, 28, 1026-1033, 1983.

575 Martin, W. R., Bender, M., Leinen, M., and Orchardo, J.: Benthic organic carbon degradation and biogenic silica dissolution in the central equatorial Pacific, Deep-Sea Research, 38, 1481-1516, 1991.

Middelburg, J. J.: A simple rate model for organic-matter decomposition in marine-sediments, Geochimica et Cosmochimica Acta, 53, 1577-1581, 1989.

Middelburg, J. J.: Reviews and syntheses: to the bottom of carbon processing at the seafloor, Biogeosciences, 15, 413-427, 10.5194/bg-15-413-2018, 2018.

580 Moodley, L., Middelburg, J. J., Soetaert, K., Boschker, H. T. S., Herman, P. M. J., and Heip, C. H. R.: Similar rapid response to phytodetritus deposition in shallow and deep-sea sediments, Journal of Marine Research, 63, 457-469, 2005.

Murray, J. W., Grundmanis, V., and Smethie, W. M.: Interstitial water chemistry in the sediments of Saanich Inlet, Geochimica et Cosmochimica Acta, 42, 1011-1026, 1978.

585 Paul, S. A. L., Gaye, B., Haeckel, M., Kasten, S., and Koschinsky, A.: Biogeochemical Regeneration of a Nodule Mining Disturbance Site: Trace Metals, DOC and Amino Acids in Deep-Sea Sediments and Pore Waters, Frontiers in Marine Science, 5, 10.3389/fmars.2018.00117, 2018.

590 Paul, S. A. L., Haeckel, M., Bau, M., Bajracharya, R., and Koschinsky, A.: Small-scale heterogeneity of trace metals including rare earth elements and yttrium in deep-sea sediments and porewaters of the Peru Basin, southeastern equatorial Pacific, Biogeosciences, 16, 4829-4849, 10.5194/bg-16-4829-2019, 2019.

Rabouille, C., and Gaillard, J.-F.: Towards the EDGE: Early diagenetic global explanation. A model depicting the early diagenesis of organic matter, O<sub>2</sub>, NO<sub>3</sub>, Mn, and PO<sub>4</sub>, Geochimica et Cosmochimica Acta, 55, 2511-2525, 1991a.

595 Rabouille, C., and Gaillard, J.-F.: A coupled model representing the deep-sea organic carbon mineralization and oxygen consumption of surficial sediments, Journal of Geophysical Research, 96, 2761-2776, 1991b.

Schriever, G., and Thiel, H.: Cruise Report DISCOL 3, Sonne cruise 7, Universität Hamburg, 59, 1992.

- Stratmann, T., Lins, L., Purser, A., Marcon, Y., Rodrigues, C. F., Ravara, A., Cunha, M. R., Simon-Lledó, E., Jones, D. O. B., Sweetman, A. K., Köser, K., and van Oevelen, D.: Abyssal plain faunal carbon flows remain depressed 26 years after a simulated deep-sea mining disturbance, *Biogeosciences*, 15, 4131-4145, 10.5194/bg-15-4131-2018, 2018a.
- Stratmann, T., Mevenkamp, L., Sweetman, A. K., Vanreusel, A., and van Oevelen, D.: Has Phytodetritus Processing by an Abyssal Soft-Sediment Community Recovered 26 Years after an Experimental Disturbance?, *Frontiers in Marine Science*, 5, 10.3389/fmars.2018.00059, 2018b.
- Sweetman, A. K., Smith, C. R., Shulse, C. N., Mailliot, B., Lindh, M., Church, M. J., Meyer, K. S., Oevelen, D., Stratmann, T., and Gooday, A. J.: Key role of bacteria in the short-term cycling of carbon at the abyssal seafloor in a low particulate organic carbon flux region of the eastern Pacific Ocean, *Limnology and Oceanography*, 64, 694-713, 10.1002/lno.11069, 2018.
- Thiel, H., and Schriever, G.: Deep-sea mining, environmental impact and the DISCOL project, *Ambio*, 19, 245-250, 1990.
- Van Oevelen, D., Moodley, L., Soetaert, K., and Middelburg, J. J.: The trophic significance of bacterial carbon in a marine intertidal sediment: Results of an in situ stable isotope labeling study, *Limnology and Oceanography*, 51, 2349-2359, 2006.
- Van Oevelen, D., Bergmann, M., Soetaert, K., Bauerfeind, E., Hasemann, C., Klages, M., Schewe, I., Soltwedel, T., and Budaeva, N. E.: Carbon flows in the benthic food web at the deep-sea observatory HAUSGARTEN (Fram Strait), *Deep-Sea Research I*, 58, 1069-1083, 2011.
- Vanreusel, A., Hilario, A., Ribeiro, P. A., Menot, L., and Arbizu, P. M.: Threatened by mining, polymetallic nodules are required to preserve abyssal epifauna, *Sci Rep*, 6, 26808, 10.1038/srep26808, 2016.
- Volz, J. B., Mogollon, J. L., Geibert, W., Arbizu, P. M., Koschinsky, A., and Kasten, S.: Natural spatial variability of depositional conditions, biogeochemical processes and element fluxes in sediments of the eastern Clarion-Clipperton Zone, Pacific Ocean, *Deep-Sea Research Part I*, 140, 159-172, 2018.
- Volz, J. B., L., H., Haeckel, M., Koschinsky, A., and Kasten, S.: Impact of small-scale disturbances on geochemical conditions, biogeochemical processes and element fluxes in surface sediments of the eastern Clarion-Clipperton Zone, Pacific Ocean, *Biogeosciences*, under review.
- Vonnahme, T. R., Molari, M., Janssen, F., Wenzhöfer, F., Haeckel, M., Titschack, J., and Boetius, A.: Effects of a deep-sea mining experiment on seafloor microbial communities and functions after 26 years, *Science Advances*, in press.
- Weber, M. E., von Stackelberg, U., Marchig, V., Wiedicke, M., and Grupe, B.: Variability of surface sediments in the Peru basin: dependence on water depth, productivity, bottom water flow, and seafloor topography, *Marine Geology*, 163, 169-184, 10.1016/s0025-3227(99)00103-6, 2000.
- Welicky, K., Suess, E., Ungerer, C. A., Müller, P. J., and Fischer, K.: Problems with accurate carbon measurements in marine sediments and particulate matter in seawater: A new approach, *Limnology and Oceanography*, 28, 1252-1259, 1983.
- Westrich, J. T., and Berner, R. A.: The role of sedimentary organic matter in bacterial sulfate reduction: The G model tested, *Limnology and Oceanography*, 29, 236-249, 1984.
- Wilson, T. R. S., Thomson, J., Colley, S., Hydes, D. J., Higgs, N. C., and Sørensen, J.: Early organic diagenesis: The significance of progressive subsurface oxidation fronts in pelagic sediments, *Geochimica et Cosmochimica Acta*, 49, 811-822, 1985.
- Witte, U., Aberle, N., Sand, M., and Wenzhöfer, F.: Rapid response of a deep-sea benthic community to POM enrichment: an in situ experimental study, *Marine Ecology Progress Series*, 251, 27-36, 2003a.
- Witte, U., Wenzhöfer, F., Sommer, S., Boetius, A., Heinz, P., Aberle, N., Sand, M., Cremer, A., Abraham, W.-R., Jørgensen, B. B., and Pfannkuche, O.: In situ experimental evidence of the fate of a phytodetritus pulse at the abyssal sea floor, *Nature*, 424, 763-766, 2003b.



## Tables

**Table 1.** Sampling station locations and description

Area	Station	Description	Latitude (S)	Longitude (W)	Water Depth / m
<b><u>Reconnaissance</u></b>					
<b>Outside DEA</b>					
		<i><b>Southern reference</b></i>			
	38 GC 1	southern reference with nodules	7°07.537'	88°27.047'	4161
	34 MUC 6	southern reference with nodules	7°07.524'	88°27.031'	4162
		<i><b>Western reference</b></i>			
	89 GC 4	western reference with nodules	7°04.562'	88°31.577'	4125
	80 MUC 22	western reference with nodules	7°04.542'	88°31.581'	4130
		<i><b>Eastern reference</b></i>			
	123 GC 6	eastern reference with(out) nodules	7°06.045'	88°24.848'	4208
	119 MUC 31	eastern reference with(out) nodules	7°06.033'	88°24.826'	4204
		<i><b>Volcano crater</b></i>			
	132 GC 7	small volcano crater with dense nodules	7°03.369'	88°26.031'	4152
	129 BC 26	small volcano crater with dense nodules	7°03.373'	88°26.026'	4144
<b>Inside DEA</b>					
		<i><b>DEA plough tracks</b></i>			
	51 GC 2	DEA west plough tracks	7°04.411'	88°27.836'	4148
	56 MUC 12	DEA west plough tracks	7°04.414'	88°27.760'	4149
	61 MUC 13	DEA west outside plough tracks	7°04.378'	88°27.781'	4148
	70 MUC 17	DEA west resettled sediment plume	7°04.400'	88°27.778'	4128
		<i><b>DEA black patch</b></i>			
	84 GC 3	DEA black patch in sidescan sonar	7°03.951'	88°27.093'	4146
	74 MUC 20	DEA black patch in sidescan sonar	7°03.945'	88°27.097'	4150
		<i><b>DEA central/trough</b></i>			
	100 GC 5	DEA central	7°04.342'	88°27.442'	4151
	108 MUC 26	DEA central	7°04.483'	88°26.919'	4169
<b><u>Microhabitats</u></b>					
		<i><b>Reference</b></i>			
	34 MUC 6	southern reference with nodules	7°07.524'	88°27.031'	4162
	80 MUC 22	western reference with nodules	7°04.542'	88°31.581'	4130
	119 MUC 31	eastern reference with(out) nodules	7°06.033'	88°24.826'	4204
		<i><b>DEA outside tracks</b></i>			
	61 MUC 13	DEA west outside plough track	7°04.378'	88°27.781'	4148
	146 ROV PC79	DEA west 20 m off plough track	7°04.4000'	88°27.8266'	4140
	166 ROV PC70	DEA east 20 m off plough track	7°04.4585'	88°26.9240'	4143
	229 MUC	DEA south outside plough track	7°04.6970'	88°27.3970'	4133
		<i><b>DEA track furrow</b></i>			
	146 ROV PC77	DEA west plough furrow	7°04.4110'	88°27.8363'	4139
	166 ROV PC69	DEA east plough furrow	7°04.4780'	88°26.9178'	4143
	219 ROV PC75	DEA south plough furrow	7°04.6930'	88°27.4540'	4155
		<i><b>DEA ridge</b></i>			
	142 ROV PC33	DEA west plough ridge	7°04.4094'	88°27.8330'	4139
	163 ROV PC83	DEA east plough ridge	7°04.4926'	88°26.9333'	4143

232 ROV PC64	DEA south plough ridge	7°04.6890'	88°27.4554'	4156
	<i><b>DEA subsurface patch</b></i>			
142 ROV PC48	DEA west subsurface patch	7°04.4113'	88°27.8127'	4140
169 ROV PC83	DEA east subsurface patch	7°04.4808'	88°26.9130'	4144
219 ROV PC58	DEA south subsurface patch	7°04.6930'	88°27.4540'	4155
	<i><b>EBS track</b></i>			
202 ROV PC80	DEA west inside EBS track	7°04.9533'	88°28.1980'	4150
202 ROV PC18	DEA west side pile EBS track	7°04.9609'	88°28.1907'	4150
211 ROV PC52	DEA west rim inside EBS track	7°04.9581'	88°28.1909'	4150
211 ROV PC73	DEA west outside of EBS track	7°04.9669'	88°28.1929'	4150

**In situ oxygen profiles**

	<i><b>Reference</b></i>			
158 LANDER-#1	Reference South	7°7.4590'	88°26.9740'	4155
	<i><b>Undisturbed DEA</b></i>			
176 ROV profiler #1	DEA E outside track	7°4.4677'	88°26.9187'	4102
169 ROV profiler #1	DEA E outside track	7° 4.4563'	88°26.9176'	4102
213 ROV profiler #2	EBS outside track	7°5.0220'	88°28.1526'	4189
146 ROV profiler #2	DEA W outside track	7°4.4000'	88°27.8274'	4140
	<i><b>DEA plough tracks</b></i>			
176 ROV profiler #2	Subsurface	7°4.4762'	88°26.9190'	4102
154 ROV profiler #2	Subsurface	7°4.4118'	88°27.8172'	4101
166 ROV profiler #2	Furrow	7°4.4898'	88°26.9286'	4104
169 ROV profiler #2	Furrow	7°4.4787'	88°26.9205'	4104
	<i><b>EBS track</b></i>			
202 ROV profiler #1	Inside track	7°4.9787'	88°28.1730'	4189

**Table 2.** Summary of analysed properties, analytical methods, estimated analytical errors, and detection limits

Parameter	Method	Error (detection limit) <sup>a</sup>
NO <sub>3</sub> <sup>-</sup>	Spectrophotometer (as sulphanile-a-naphthylamide) <sup>b</sup>	(1 µmol l <sup>-1</sup> )
NO <sub>2</sub> <sup>-</sup>	Spectrophotometer (as sulphanile-a-naphthylamide) <sup>b</sup>	(1 µmol l <sup>-1</sup> )
NH <sub>4</sub> <sup>+</sup>	Spectrophotometer (as indophenol blue) <sup>b</sup>	(1 µmol l <sup>-1</sup> )
Mn <sup>2+</sup>	ICP-AES	5-10% (1 µmol l <sup>-1</sup> )
SO <sub>4</sub> <sup>2-</sup>	Ion chromatography	0.8-1.2 mmol l <sup>-1</sup> (5 mmol l <sup>-1</sup> )
C <sub>org</sub>	CHN-Analyser <sup>c</sup>	0.04 wt%
Alkalinity	Titration <sup>d</sup>	0.05 meq l <sup>-1</sup>
Porosity	Weight difference before and after drying of the sediment	0.02

<sup>a</sup> Note. For some properties no analytical error could be determined because of few data points or concentrations close to the detection limit.

<sup>b</sup> Grasshoff et al. (1999).

<sup>c</sup> Welicky et al. (1983).

<sup>d</sup> Breland and Byrne (1993).

**Table 3.** Reaction stoichiometry and rate expressions of the organic mater  $((CH_2O)_a(NH_3)_b(H_3PO_4)_c)$  degradation and secondary redox reactions. All solute species are in concentrations of  $\frac{mmol}{L_{pw}}$  and all solid species in  $\frac{mmol}{L_{ds}}$ . All reaction rate expressions are stated in the units of  $\frac{mmol}{L_{pw} a}$  via a conversion with  $F_{pw} = \left(\frac{1-\phi}{\phi}\right)$ .

ID	Reaction	Rate expression (mmol/Lpw/a)
<b>Organic matter degradation</b>		
	$(CH_2O)_a(NH_3)_b(H_3PO_4)_c + (a + 2b)O_2$ $+ (b + 2c)HCO_3^- \rightarrow (a + b + 2c)CO_2$ $+ (b)NO_3^- + (c)HPO_4^{2-}$ $+ (a + 2b + 2c)H_2O$	$\sum_{i=1,2,3} k_i \frac{Cor g_i}{a} R_{O_2} F_{pw}$
	$(CH_2O)_a(NH_3)_b(H_3PO_4)_c + \left(\frac{4}{5}a + \frac{3}{5}b\right)NO_3^-$ $\rightarrow \frac{1}{2}\left(\frac{4}{5}a + \frac{3}{5}b + b\right)N_2 + cHPO_4^{2-}$ $+ \left(\frac{3}{5}a + \frac{6}{5}b + 2c\right)H_2O$ $+ \left(\frac{1}{5}a - \frac{3}{5}b + 2c\right)CO_2$ $+ \left(\frac{4}{5}a + \frac{3}{5}b - 2c\right)HCO_3^-$	$\sum_{i=1,2,3} k_i \frac{Cor g_i}{a} R_{NO_3} F_{pw}$
	$(CH_2O)_a(NH_3)_b(H_3PO_4)_c + 2aMnO_2 + (3a + b - 2c)CO_2$ $+ (a + b - 2c)H_2O$ $\rightarrow (4a + b - 2c)HCO_3^- + 2aMn^{2+}$ $+ bNH_4^+ + cHPO_4^{2-}$	$\sum_{i=1,2,3} k_i \frac{Cor g_i}{a} R_{MnO_2} F_{pw}$
<b>Secondary redox reactions</b>		
	$NH_4^+ + 2O_2 + 2HCO_3^- \rightarrow NO_3^- + 2CO_2 + 3H_2O$	$k_{NH_4Ox} NH_4 O_2$
	$2Mn^{2+} + O_2 + 4HCO_3^- \rightarrow 2MnO_2 + 4CO_2 + 2H_2O$	$k_{MnOx} Mn^{2+} O_2$
	$4Fe(II) + O_2 + 2H_2O + 4CO_2 \rightarrow 4Fe(III) + 4HCO_3^-$	$k_{Fe(II)Ox} Fe^{2+} O_2$

**Monod expressions**

$$R_{O_2} = \frac{O_2}{K_{O_2} + O_2}$$

$$R_{NO_3} = \frac{NO_3}{K_{NO_3} + NO_3} \frac{K_{O_2}}{K_{O_2} + O_2}$$

$$R_{MnO_2} = \frac{MnO_2}{K_{Mn} + MnO_2} \frac{K_{NO_3}}{K_{NO_3} + NO_3} \frac{K_{O_2}}{K_{O_2} + O_2}$$

**Table 4.** Constrained and fitted parameters used in the numerical simulations

Parameter	Value	Units	Reference
<b>General parameter</b>			
Temperature	4	°C	a)
Pressure	400	bar	a)
Salinity	35	‰	a)
Redfied ratio (C:N:P)	106:16:01		
Sedimentation rate	0.0004	cm a <sup>-1</sup>	Haeckel et al. (2001)
Maximu depth of calculation	200	cm	
Number of points in the numerical grid (uneven)	500		
<b>Fitted parameters - background (reference) model</b>			
Porosity at sediment surface ( $\phi_0$ )	0.94		c)
Porosity at infinite depth ( $\phi_\infty$ )	0.86		c)
Porosity attenuation coefficient ( $\beta$ )	0.14		c)
Bioturbation coefficient ( $D_b^0$ )	0.65	cm <sup>2</sup> a <sup>-1</sup>	b)
Bioturbation half depth ( $x_{Db}$ )	10	cm	b)
Bioturbation decrease ( $\beta_{Db}$ )	4		b)
Flux of labile C <sub>org</sub> ( $F_{G0}$ )	10	μmol cm <sup>-2</sup> a <sup>-1</sup>	c)
Flux of semi-labile C <sub>org</sub> ( $F_{G1}$ )	1.2	μmol cm <sup>-2</sup> a <sup>-1</sup>	c)
Flux of refractory C <sub>org</sub> ( $F_{G2}$ )	0.06	μmol cm <sup>-2</sup> a <sup>-1</sup>	c)
Rate constant for labile C <sub>org</sub> oxidation ( $k_{G0}$ )	0.1	a <sup>-1</sup>	c)
Rate constant for semi-labile C <sub>org</sub> oxidation ( $k_{G1}$ )	0.003	a <sup>-1</sup>	c)
Rate constant for refractory C <sub>org</sub> oxidation ( $k_{G2}$ )	5E-07	a <sup>-1</sup>	c)
Rate constant for reaction of Mn <sup>2+</sup> and O <sub>2</sub>	1E+06	l mmol <sup>-1</sup> a <sup>-1</sup>	c)
Rate constant for reaction of NH <sub>4</sub> <sup>+</sup> and O <sub>2</sub>	500	l mmol <sup>-1</sup> a <sup>-1</sup>	c)
Monod constant for O <sub>2</sub> reduction	8E-06	mmol	c)
Monod constant for NO <sub>3</sub> <sup>-</sup> reduction	0.03	mmol	Boudreau (1996)
Monod constant for MnO <sub>2</sub> reduction	10	mmol	Boudreau (1996)
[MnO <sub>2</sub> ] <sub>model domain</sub>	1.9	wt%	a)
[O <sub>2</sub> ] <sub>bottom water</sub>	0.132	mmol l <sup>-1</sup>	a)
[NO <sub>3</sub> <sup>-</sup> ] <sub>bottom water</sub>	0.042	mmol l <sup>-1</sup>	a)
[NH <sub>4</sub> <sup>+</sup> ] <sub>bottom water</sub>	0	mmol l <sup>-1</sup>	a)
[Mn <sup>2+</sup> ] <sub>bottom water</sub>	0	mmol l <sup>-1</sup>	a)
[Alkallinity] <sub>bottom water</sub>	2.4	meq l <sup>-1</sup>	a)
[Mn <sup>2+</sup> ] <sub>lower boundary</sub>	0.05	mmol l <sup>-1</sup>	a)
<b>Parameter for impact simulations</b>			
Bioturbation recovery time ( $t_{DB}$ )	100 / 200	a	d)
<b>Case 'reactive Fe(II)-O<sub>2</sub> layer'</b>			
[Fe(II)] at lower boundary	0.44	wt%	e)
Fe(II) half depth of increase	20	cm	
Fe(II) profile reduction coefficient	2		
Rate constant for reaction of Fe(II) and O <sub>2</sub>	100	l mmol <sup>-1</sup> a <sup>-1</sup>	c)
<b>Case 'removal'</b>			
Removed sediment thickness	10	cm	d)
<b>Case 'O<sub>2</sub> flooding'</b>			
[O <sub>2</sub> ] <sub>reactive layer</sub>	= [O <sub>2</sub> ] <sub>bottom water</sub>	mmol l <sup>-1</sup>	
Half depth O <sub>2</sub> decrease	12	cm	

O <sub>2</sub> attenuation coefficient	2.5		
<b><i>Bioturbation model</i></b>			
<sup>210</sup> Pb radioactive decay constant	ln(2)/22.3	a <sup>-1</sup>	
<sup>226</sup> RaTh radioactive decay constant	ln(2)/1602	a <sup>-1</sup>	
<sup>230</sup> Th radioactive decay constant	ln(2)/57380	a <sup>-1</sup>	
[ <sup>210</sup> Pb] <sub>bottom water</sub>	1.0	Bq g <sup>-1</sup>	b)
[ <sup>226</sup> Ra] <sub>bottom water</sub>	0.3	Bq g <sup>-1</sup>	b)
[ <sup>230</sup> Th] <sub>bottom water</sub>	0.6	Bq g <sup>-1</sup>	b)
<hr/> a) Approximated by field data; b) fitted to Pb data (Figure 7); c) fitted to field data; d) Approximated from data and references presented in Volz et al. (submitted); e) Inferred from data presented in König et al. (1997, 1999) <hr/>			

665

670

## Figures

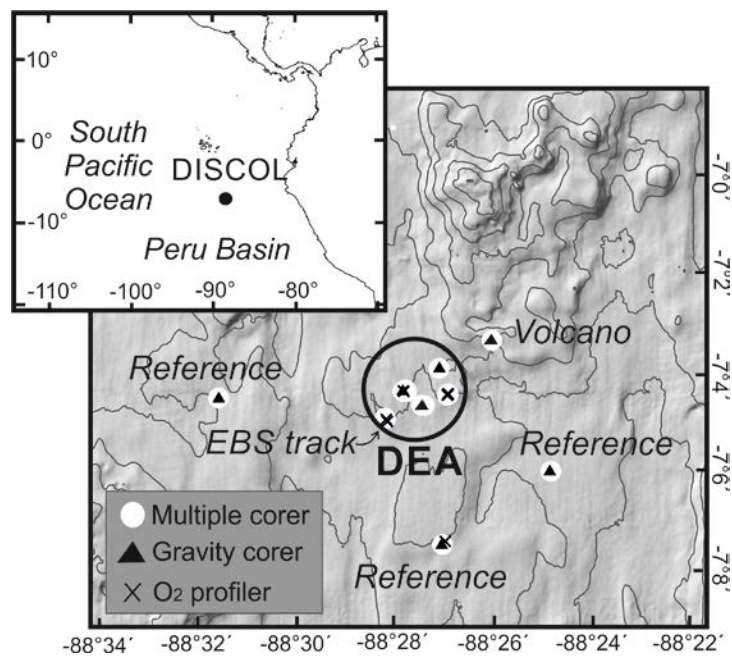


**Figure 1.** Bathymetric map of the DEA region in the Peru basin including the sampling stations presented in this work. More details on the sampling locations are provided in Table 1.

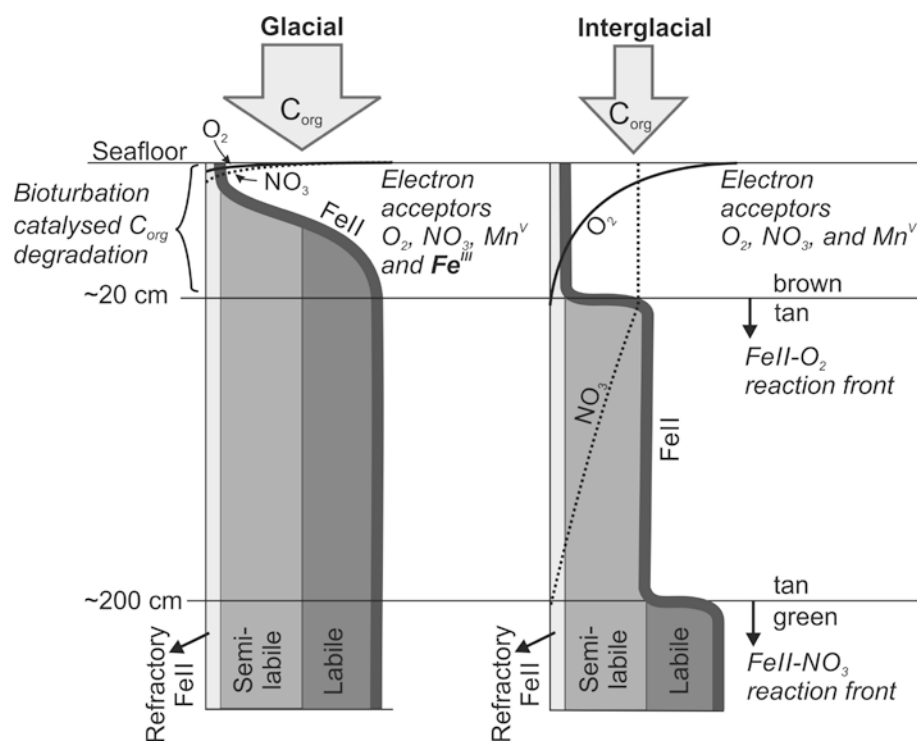


**Figure 2.** Schematic diagram (not to scale) outlining the formation of a Fe(II) rich clay phase (green) in the context of glacially high organic matter input and its conversion to Fe(III) by downward progressing  $NO_3$  fronts during interglacial periods triggered by reduced organic matter input as postulated by König et al. (2001). In this study, we propose that a second reaction front exists impeding the downward  $O_2$  migration through a reaction with the semi-labile Fe(II) phase.



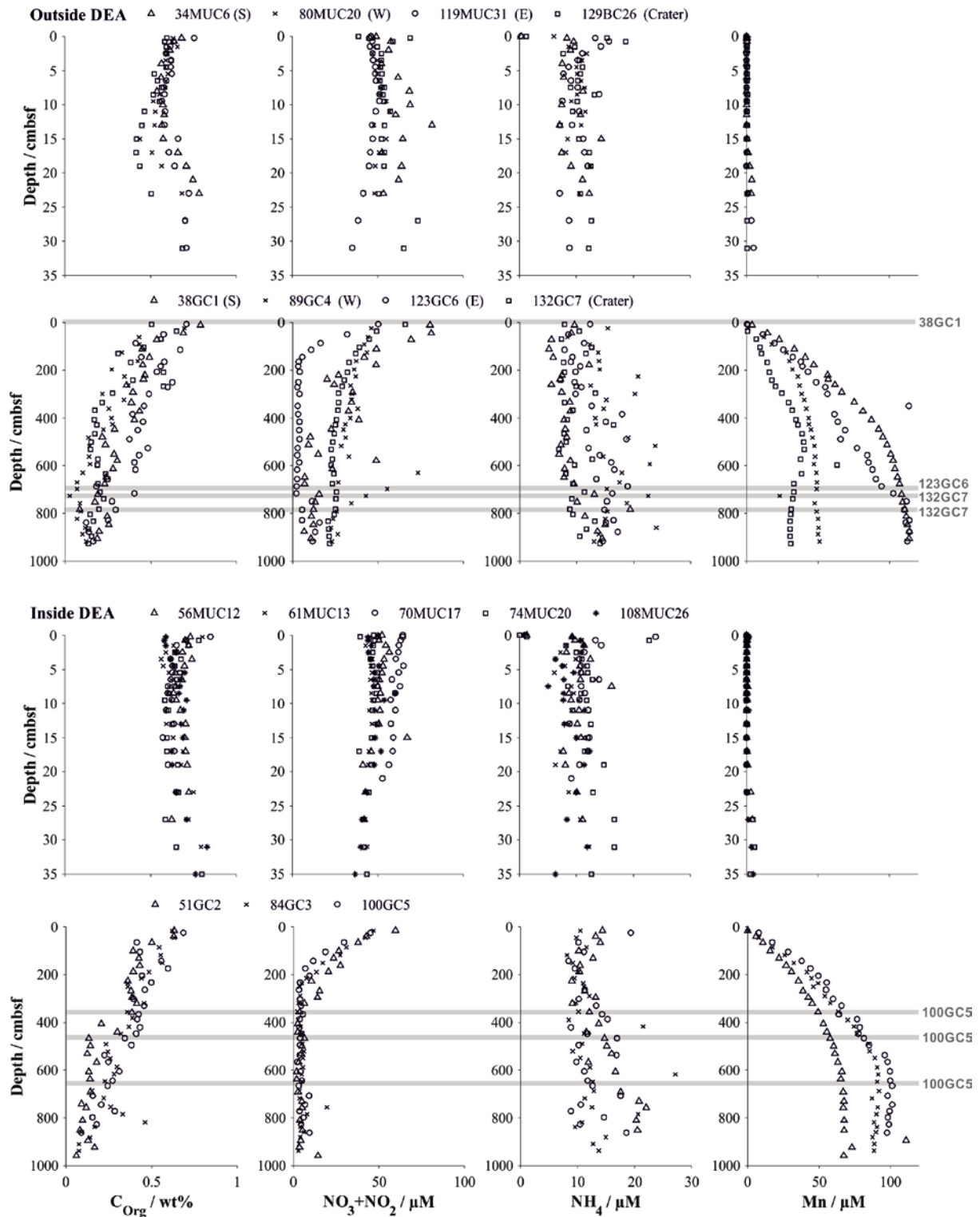
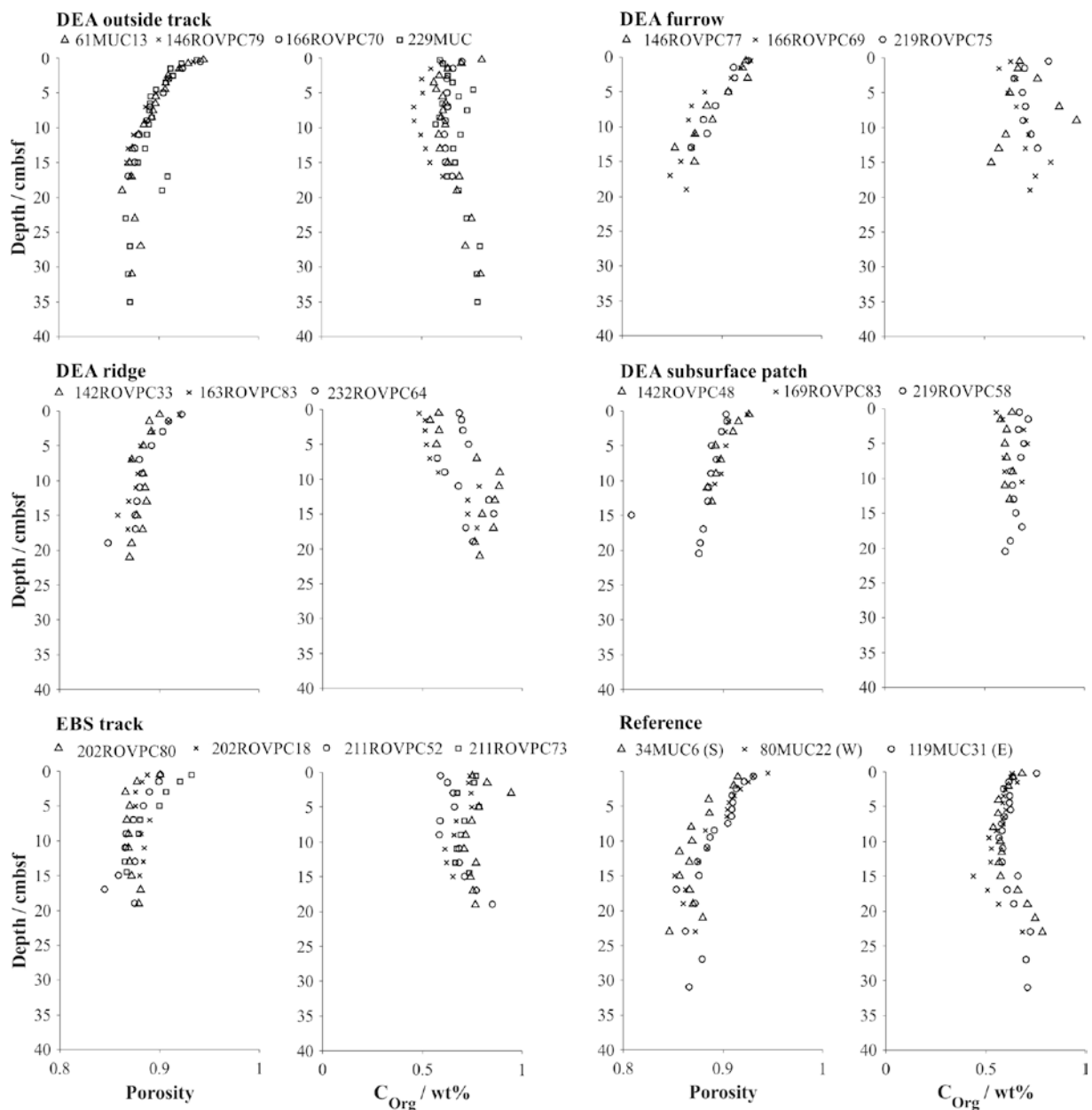


**Figure 3.** Organic carbon content (Paul et al., 2018; Paul et al., 2019) and dissolved solute profiles of summed  $\text{NO}_3$  and  $\text{NO}_2$  (Paul et al., 2018; Paul et al., 2019),  $\text{NH}_4$  and Mn in gravity cores and their corresponding multicores. Symbols represent the measured values at the mean depth of the sediment layer sampled. Buried manganese nodules are indicated by a grey line. Details on individual sampling stations can be found in Table 1.



695 **Figure 4.** Porosity and organic carbon content in multi- and box-corer retrieved in various microhabitats (Paul et al., 2018). Symbols represent the measured values at the mean depth of the sediment layer sampled. Details on individual sampling stations can be found in Table 1.

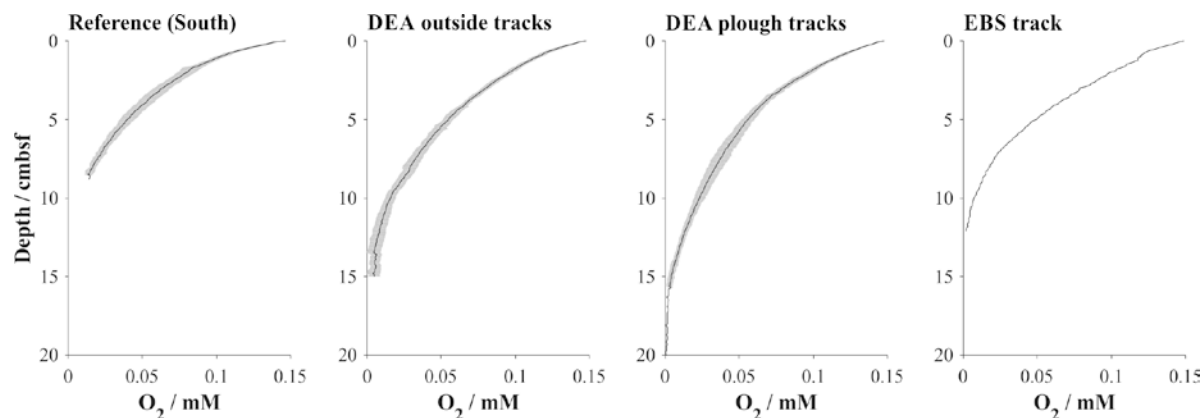


**Figure 5.** Averaged (black line) in situ oxygen profile representative of various disturbance settings including their standard deviations (shaded area). Because the depth steps between each measuring point of the oxygen profiles are very close, they are not resolved in the diagram. Details on individual sampling stations can be found in Table 1.

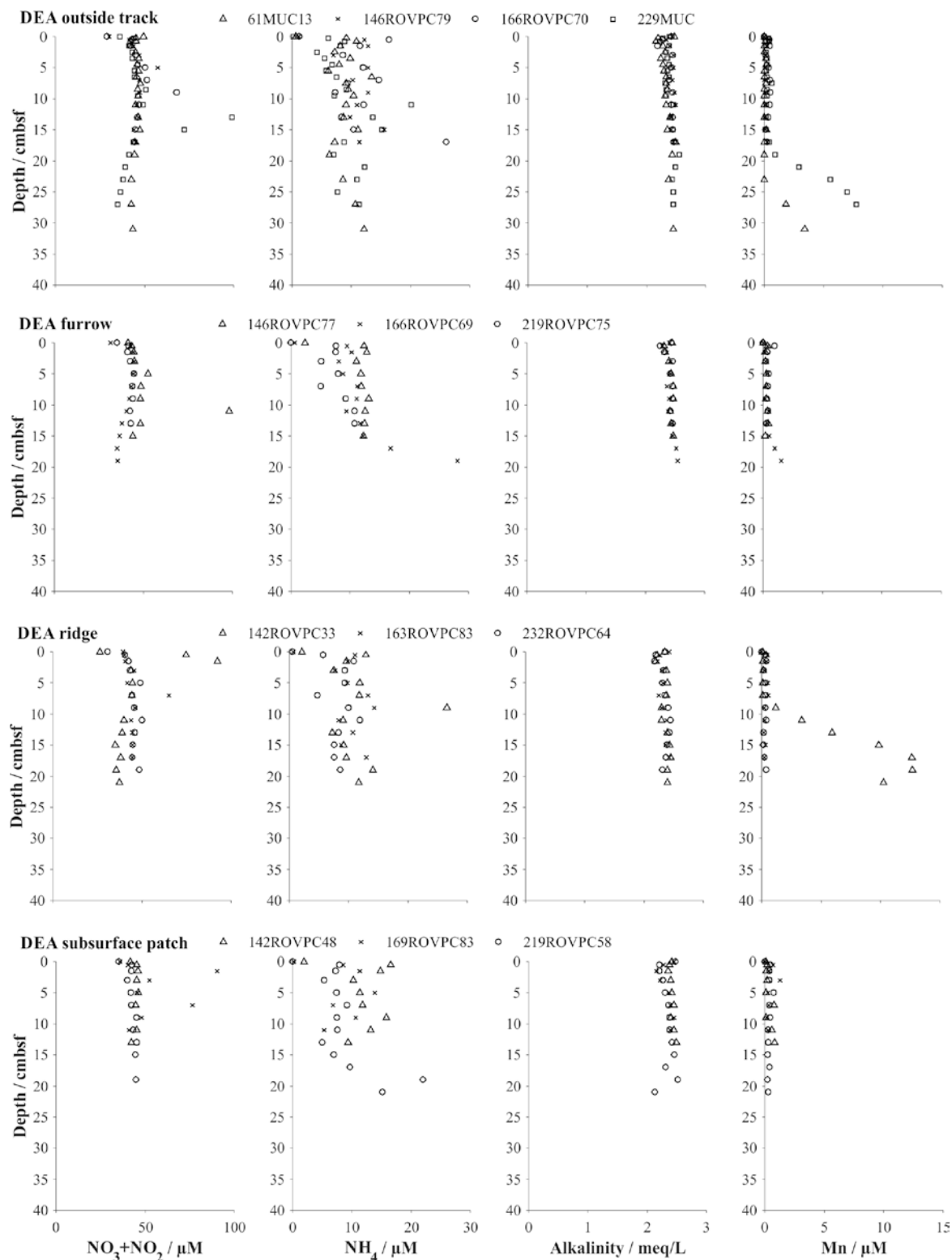


**Figure 6.** Solute profiles in multi- and box-corer retrieved in various microhabitats (. Symbols represent the measured values at the mean depth of the sediment layer sampled (summed  $\text{NO}_3$  and  $\text{NO}_2$  from Paul et al. (2018)). Details on individual sampling stations can be found in Table 1.

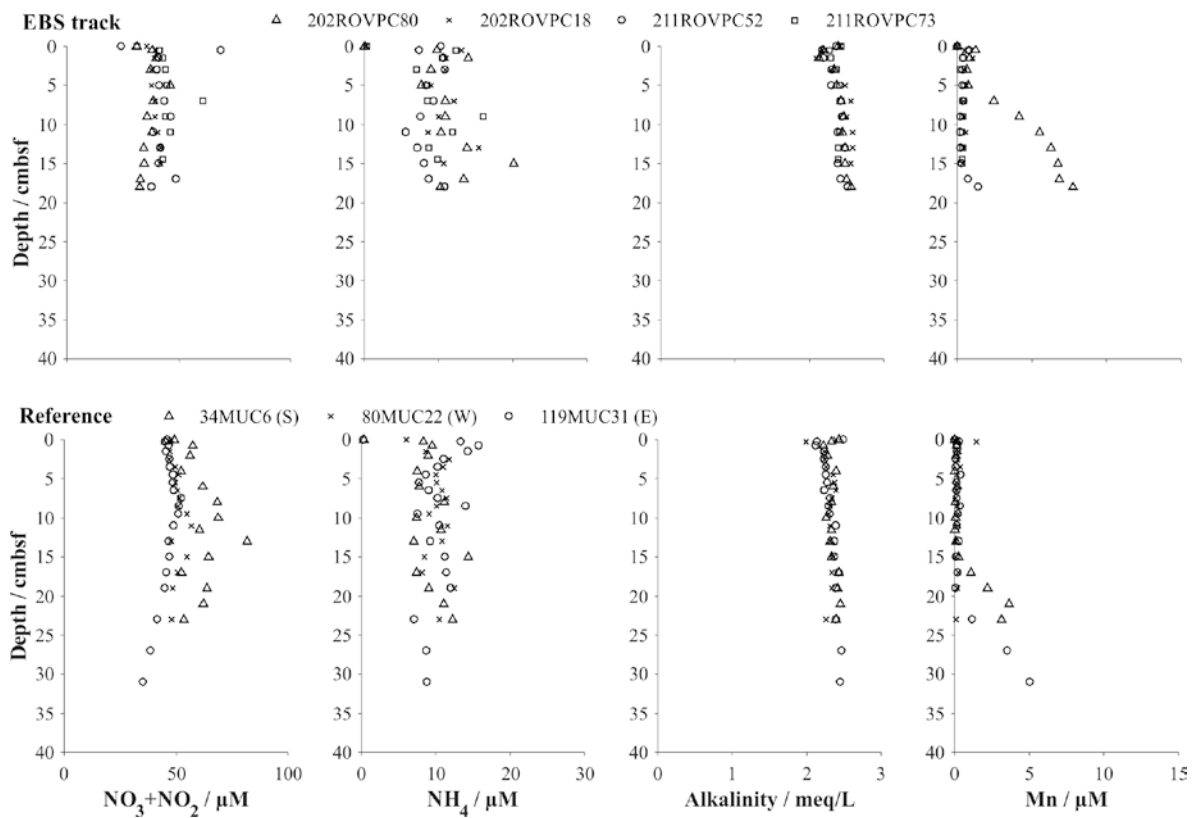
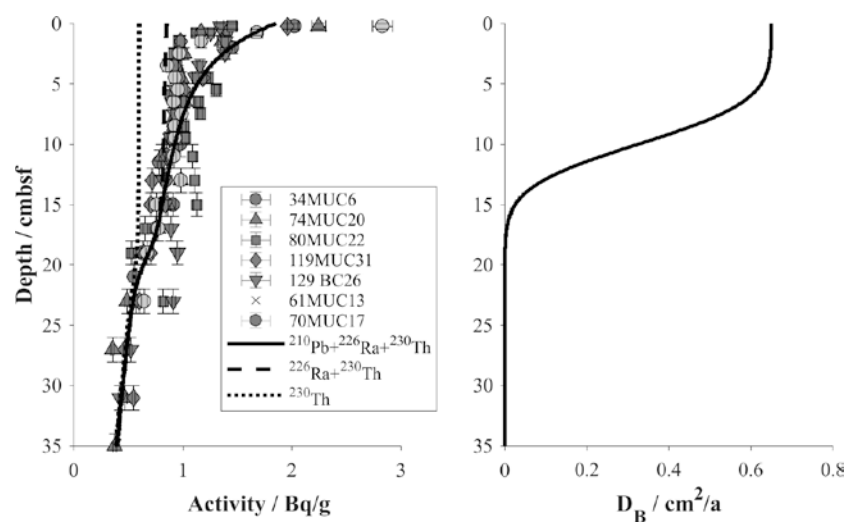
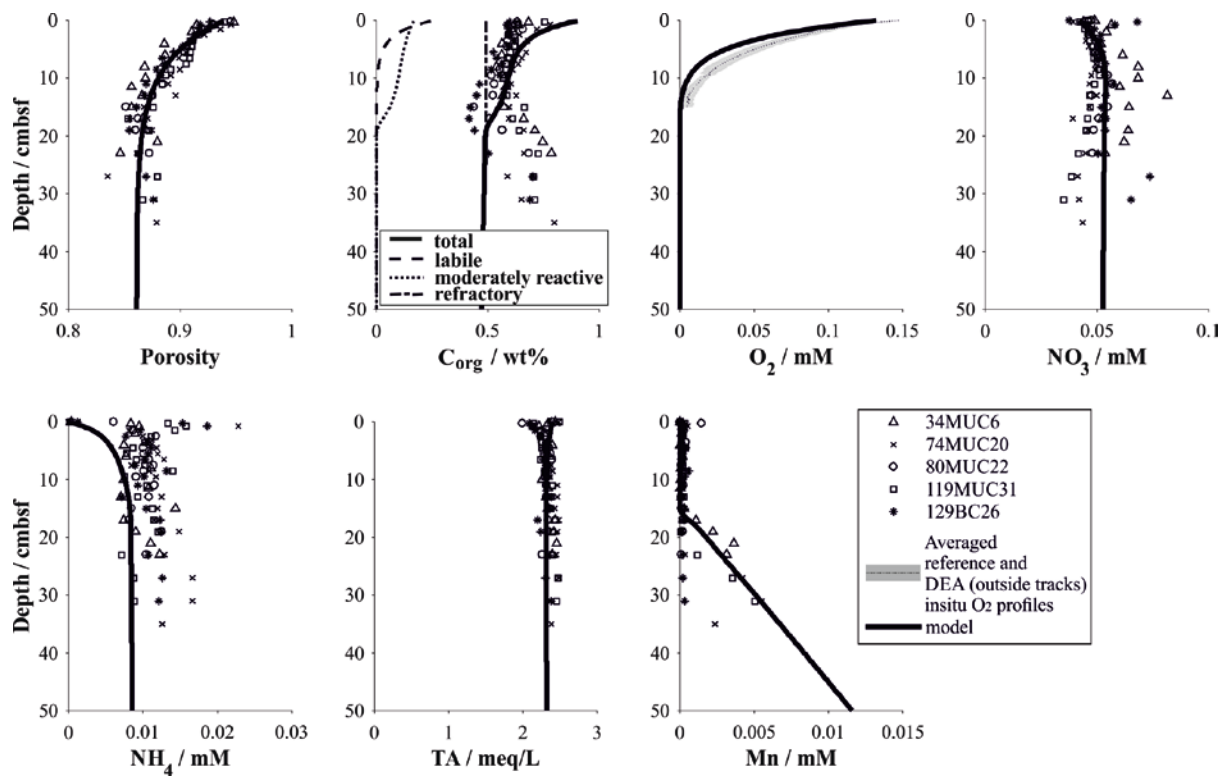


Figure 6. Cont'd.



**Figure 7.** Model results of the faunal bioturbation activity in reference and DEA-outside track sediments based on measured  $^{210}\text{Pb}$  activities. Left: Model curves indicate total  $^{210}\text{Pb}$  activity (solid) and supported contributions by  $^{230}\text{Th}$  (dotted) and  $^{226}\text{Ra}$  (dashed minus dotted). Right: Bioturbation intensity profile derived for the background model.



**Figure 8.** Simulation of background biogeochemical processes and their effect on solute profiles in the DEA region. In addition to the three reference stations, two other undisturbed sites were included for comparison. See

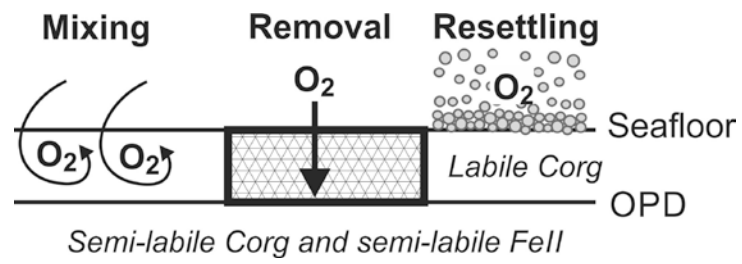


**Figure 9.** Schematic characterization of the different impact types at a mined seafloor and their influence on  $O_2$  distribution.



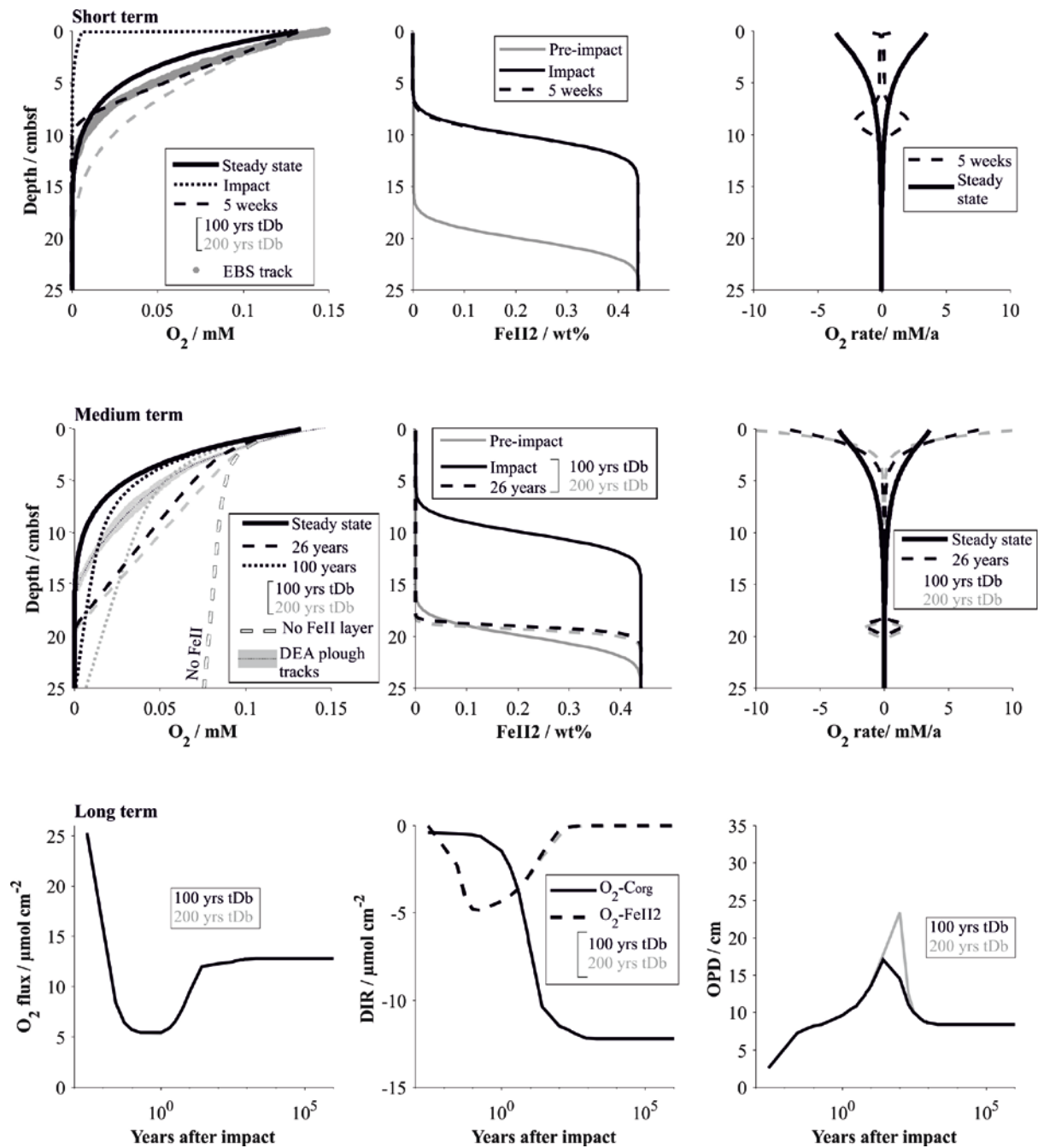


**Figure 10.** Impact simulations after a disturbance causing the reactive upper 10 cm to be removed. The short term (up to 5 weeks, comparable to the EBS tracks) and medium term (26 years, comparable to the DEA tracks) impact is visualized by the respective  $O_2$  profiles and the fluxes shaping the  $O_2$  profiles. It is assumed that the oxygen penetration depth is impeded by a reactive Fe(II) layer. Note, the Fe(II) is assumed to be located at 20 cmbsf but is placed at 10 cm if the upper 10 cm are removed. For comparison the  $O_2$  profile in the absence of a Fe(II) layer is also shown. The long term impact is demonstrated by the surface flux of oxygen into the sediment, the depth integrated reaction rates (DIR) of oxygen with organic matter ( $C_{org}$ ) and with the reactive Fe(II) layer, as well as the oxygen penetration depth (OPD) over time. The influence of the bioturbation recovery time is shown by plotting the lines that correspond to a recovery interval of 100 and 200 years in black and grey respectively.

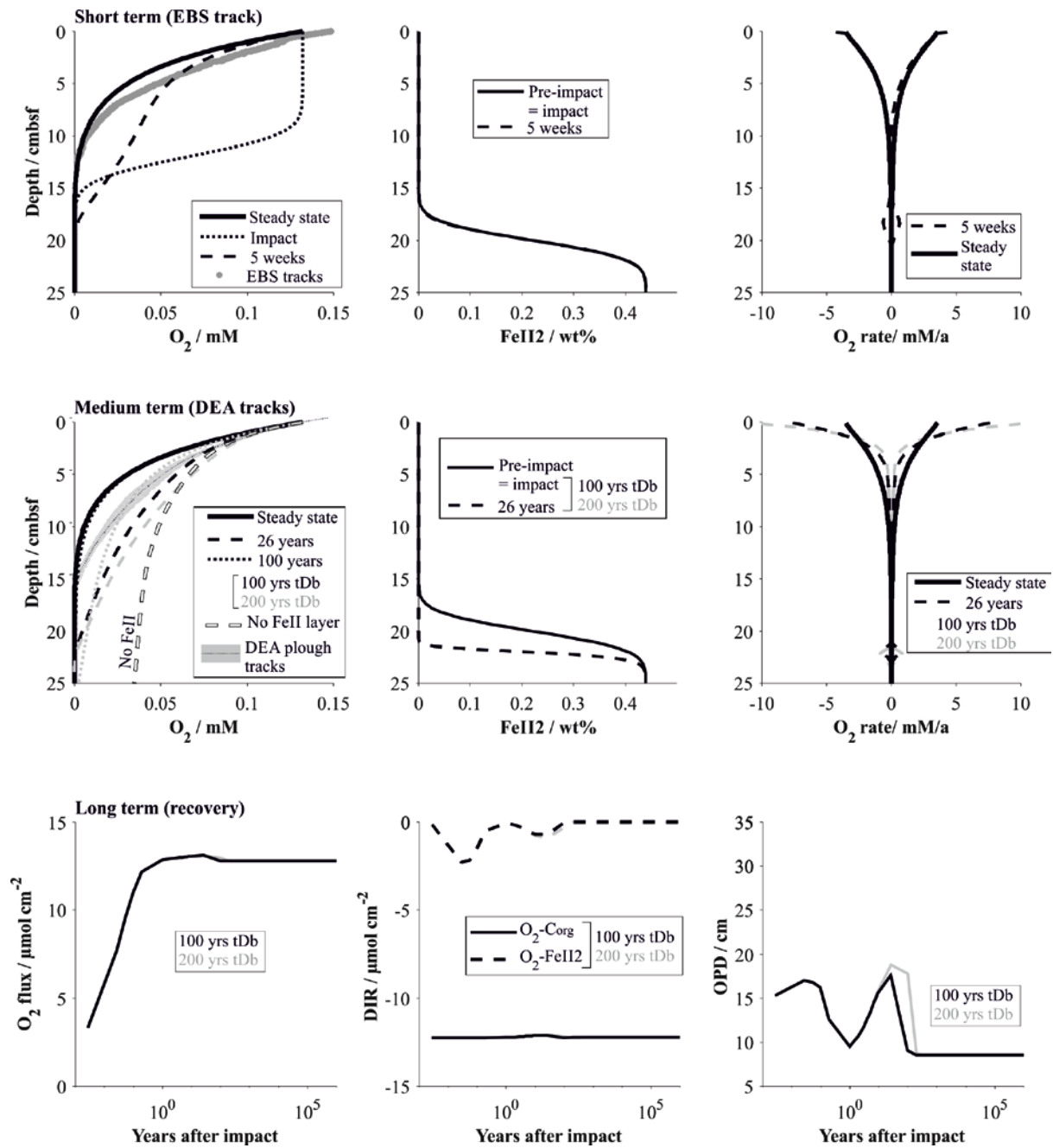


**Figure 11.** Impact simulations after a disturbance causing the upper sediment layer to be exposed to bottom water oxygen levels (i.e. through mixing or by resettling sediments, see Figure 9). See the caption of Figure 10 for details.

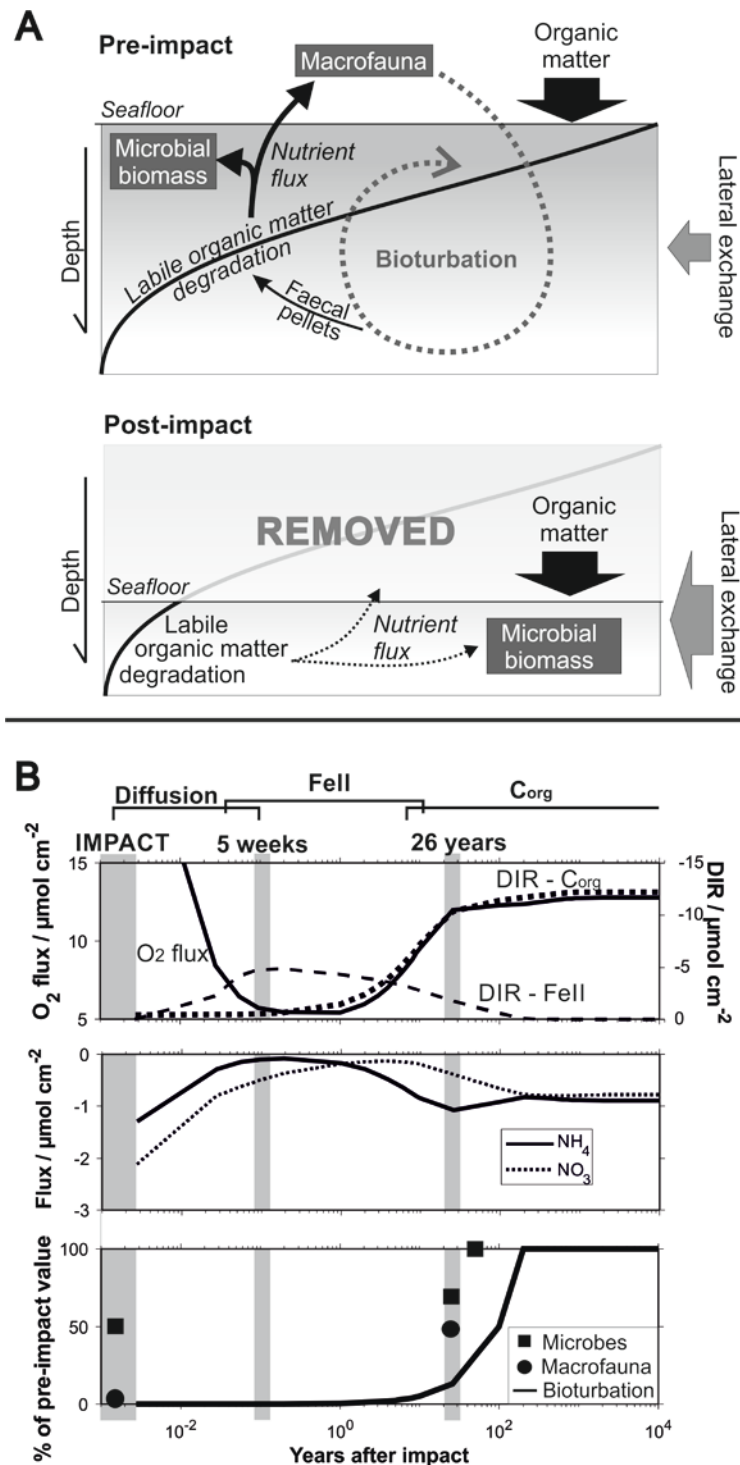


**Figure 12.** (A) Schematic diagram showing the delicate interplay between the distribution of organic matter, microbial activity and the bioturbation through burrowing megafauna in a pre-impact system and after removal of the upper reactive sediment layer. (B) Quantitative comparison of geochemical and biological processes over time after an impact through sediment removal. Biological data is taken from Stratmann et al. (2018a) (Macrofaunal abundance) and Vonnahme et al. (in press) (microbial cell count) for the most severely disturbed sites (e.g. inside 5 weeks old EBS tracks, and inside 26 years old plough marks).